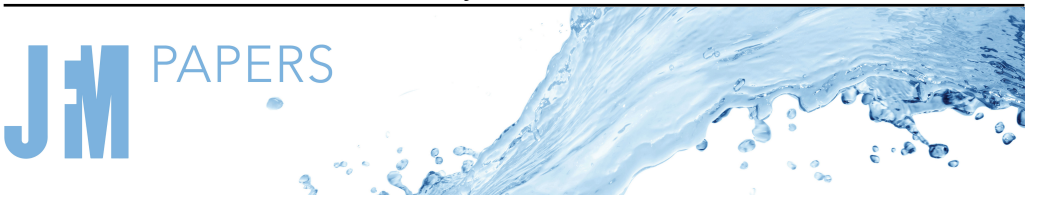
J. Fluid Mech. (2026), *vol.* 1037, A13, doi:10.1017/jfm.2026.11637



The yield limit for a single bubble trapped in a damaged viscoplastic fluid

Anita Hadizadeh[1] **and Ian A. Frigaard**[1,2]

[1]Department of Mechanical Engineering, University of British Columbia, 2054-6250 Applied Science Lane, Vancouver, BC V6T 1Z4, Canada

[2]Department of Mathematics, University of British Columbia, 1984 Mathematics Road, Vancouver, BC V6T 1Z2, Canada

Corresponding author: Ian A. Frigaard, frigaard@math.ubc.ca

(Received 18 January 2026 UTC; revised 1 May 2026 UTC; accepted 1 May 2026 UTC)

Bubbles rising in yield-stress fluids leave behind pathways in the memory of the fluid. These in turn influence the trajectories of subsequent bubbles released. Qualitatively, the effect manifests as a damaged pathway, modelled here as a low-viscosity Newtonian fluid within the surrounding viscoplastic fluid. Secondary bubbles are attracted towards these pathways, as is observed computationally and experimentally. Here we explore the effect of a damaged path on the release of a trapped bubble, captured by the critical yield number Y_c. We show that proximity to a damaged path increases Y_c, but eventually beyond a critical distance there is no influence on Y_c. We explore the effects of shape and surface tension on the aforementioned proximity results.

Key words: bubble dynamics, low-Reynolds-number flows, plastic materials

1. Introduction

Viscoplastic materials behave as rigid solids when the applied stress is below a critical value and as fluids once that threshold is exceeded (Balmforth, Frigaard & Ovarlez 2014). As such, small gas bubbles which generate small buoyancy forces tend to become trapped in these materials during preparation and processing flows, intentionally or otherwise. Our concern here is with gas bubbles that arise from bacterial digestive processes within yield-stress media, i.e. bubbles that form and grow *in situ*. As they grow, the buoyancy force eventually overcomes restraining forces from the yield stress and the bubbles start to rise. This may happen within naturally formed 'muck' at the bottom of lakes and ponds, or as a result of industrial activity. In either case, a concern is the contribution to greenhouse

© The Author(s), 2026. Published by Cambridge University Press. This is an Open Access article, distributed under the terms of the Creative Commons Attribution licence (https://creativecommons.org/licenses/by/4.0/), which permits unrestricted re-use, distribution and reproduction, provided the original article is properly cited.

https://doi.org/10.1017/jfm.2026.11637 Published online by Cambridge University Press

gas emissions and similar negative environmental effects. Hence, these effects need to be quantified.

Our specific motivation comes from bubble trapping and release in oil sands tailings ponds (Small *et al.* 2015; He *et al.* 2024). These large ponds contain tailings tens of metres deep and extend over many square kilometres. The tailings are colloidal suspensions that stratify in the pond as a result of solids settling. Larger solids fall through the liquid, but particles in the sub-20 μm range have body forces typically dominated by attractive colloidal forces, hence forming a yield-stress material. The rheology may be estimated from model correlations (Wells & Kaminsky 2015), from laboratory testing (e.g. Derakhshandeh 2016; Piette *et al.* 2022) or eventually from micro-mechanical models (Kapur *et al.* 1997; Scales *et al.* 1998); see also (Wang *et al.* 2014). *In situ* the density, solids content (clays, fines and coarse sand), clay-to-water ratio and yield stress will all stratify depthwise (Hajieghrary & Frigaard 2024). However, this stratification occurs on length scales long with respect to bubble size, making the approximation of a bubble in uniform yield-stress fluid reasonable.

Residual bitumen and naphtha are digested within the ponds, generating CO_2 and CH_4, eventually forming bubbles, observed at the pond surface. Various fluid mechanical aspects of the process have been studied, such as ebullition, mixing and entrainment across interfaces (Lawrence, Tedford & Pieters 2016; Tedford *et al.* 2019; Zhao *et al.* 2022; Zare, Frigaard & Lawrence 2024), all with a view to better managing/controlling process impacts. Here our focus is on a different problem: understanding the onset of bubble motion, i.e. trapping and release.

Quantifying the onset of motion of a bubble trapped in a yield-stress fluid is central to predicting gas emissions. The theoretical foundation for this problem was established by Dubash & Frigaard (2004), who formulated the mobility flow problem and defined the critical yield number, Y_c, marking the onset of bubble motion. Putz & Frigaard (2010) and Chaparian & Frigaard (2017) extended this approach to rigid particles settling in a yield-stress fluid, using resistance and mobility formulations, and exploring the limiting energy balances near Y_c. These analyses assumed a homogeneous Bingham fluid rheology, although all simple yield-stress fluids give the same Y_c. Later, Pourzahedi *et al.* (2022) used high-resolution augmented-Lagrangian (AL) simulations to compute Y_c for single bubbles of varying aspect ratio and surface tension, providing benchmark data for the present study. The first direct experimental study of flow onset (Daneshi & Frigaard 2023) revealed changes in Y_c with bubble shape that were qualitatively consistent with those in Pourzahedi *et al.* (2022). With a view to application, where many bubbles are present in a tailings pond, bubble clouds were studied computationally in two dimensions by Chaparian & Frigaard (2021) and experimentally by Daneshi & Frigaard (2024), who examined the sensitivity of yielding/onset to bubble geometry, distribution and volume (area) fraction.

While the above studies represented a logical progression in developing our understanding, they were based on the idealisation of randomly distributed bubbles in an inelastic viscoplastic liquid, at varying (likely low) volume fractions. Experimental insight has slowly chipped away at this image, leading to the current study. First was the observation that the computed steady rise shapes of bubbles in ideal viscoplastic fluids (Tsamopoulos *et al.* 2008; Dimakopoulos, Pavlidis & Tsamopoulos 2013) did not produce experimentally observed tail shapes and wake patterns. These shapes and effects were found only more recently by Moschopoulos *et al.* (2021), who considered elastoviscoplastic (EVP) constitutive laws as the basis of their study.

Second was the observation that experimental repeatability using fluids such as Carbopol often required the fluids to be re-sheared/mixed between bubble releases.

https://doi.org/10.1017/jfm.2026.11637 Published online by Cambridge University Press

In particular, waiting for typical (viscoelastic) relaxation times did not remove the 'memory' of previous bubbles. Thus, resetting the fluid has been a common feature of many experimental bubble studies (Dubash & Frigaard 2007; Sikorski, Tabuteau & de Bruyn 2009; Lopez *et al.* 2018; Wang *et al.* 2019), and also earlier in the context of studying settling particles (Atapattu, Chhabra & Uhlherr 1995; Gheissary & Van Den Brule 1996). While initially these effects have been seen as an experimental inconvenience, later it has become apparent that they contain many interesting and important phenomena. Zare & Frigaard (2018) studied gas invasion into a column of Carbopol, driven under pressure through a nozzle. The bubble volume was not preset, but determined by a break-off process, influenced by the fluid rheology close to the nozzle. It was observed that the bubbles that formed/invaded after the initial bubble were consistently smaller than the first bubble, but also travelled upwards faster. This is consistent with the notion that the shearing in some way has 'damaged' the surrounding fluid. In earlier work, Mougin, Magnin & Piau (2012) showed that successive bubbles effectively sheared a confined channel through the fluid, outside of which there was little deformation. In an elegant experiment, Lopez *et al.* (2018) sheared their fluid by drawing a solid rod through it, at an angle to the vertical. Remarkably, subsequent released bubbles translated along the path where the rod had been.

Inspired by Mougin *et al.* (2012) and Lopez *et al.* (2018), in Zare, Daneshi & Frigaard (2021) we further explored the effects of non-uniform rheology on an actual bubble flow. Essentially, this meant ignoring exactly how the fluid became 'damaged' (i.e. rheologically), and looking at bubble dynamics in model two-liquid systems: a background yield-stress fluid (Bingham) and a damaged Newtonian layer of smaller viscosity. Using transient two-dimensional (2-D) computations and a regularisation method, bubbles released close to the damaged layer were found to approach the layer, become enveloped in it and travel upwards within the layer, at accelerated speeds and often elongating. Experiments confirmed these phenomena. Inclined damaged channels/pathways were also studied, computationally and experimentally, showing that bubbles could translate laterally even along strongly inclined damaged channels.

Around this time, we also became aware of field studies (Bussmann *et al.* 2011; Zhao *et al.* 2021), where 'pockmarks' were observed in a sediment layer between a clear water cap and tailings suspension below. These circular holes are believed to be venting structures for the bubbles below. In the images of Zhao *et al.* (2021) the holes appear as entrances to a watery tunnel below, as was subsequently studied in the laboratory (Zhao *et al.* 2022). This and the aforementioned studies in Zare *et al.* (2021) led to a reappraisal of the supposed subsurface bubble dynamics. Even if the initially nucleated bubbles are dispersed approximately uniformly and grow independently, it seemed likely that the release of bubbles and the paths followed to the surface would be influenced by the stress history of adjacent old pathways, i.e. promoting lateral migration and joining of pathways. The pockmarks and underlying tunnels may be indicators of a rootlike structure of bubble paths to the surface, repeatedly exiting through the same pockmarks.

This hypothesised structure has led to our current interest to quantify better the influence of adjacent damaged pathways on bubble release and passage. On release from entrapment there is an interest to assess the degree to which bubbles approach a damaged path. Recently, we studied this question experimentally (Goral & Frigaard 2025), creating a 2-D 'damaged layer' by mechanically inserting a plate into and withdrawing it from a yield-stress-fluid bath, then releasing bubbles at different distances from the layer. The released bubbles were observed to migrate preferentially towards the damaged layer, as could be fitted by a simple toy model.

https://doi.org/10.1017/jfm.2026.11637 Published online by Cambridge University Press

Regarding the actual bubble release, if an adjacent path results in a higher Y_c value than in a uniform liquid, then bubbles will mobilise at smaller size. These in turn will create their own stress histories affecting further bubbles. Therefore, understanding how proximity affects Y_c is of key importance in assessing the growing influence of damaged pathways. This is the topic of this paper. We determine the onset conditions for a single bubble rising in a damaged viscoplastic fluid, using an AL formulation. Section 2 presents the problem definition and governing equations. Section 3 outlines the numerical implementation and § 4 discusses the effects of offset distance, bubble aspect ratio, surface tension and viscosity ratio on the critical yield number Y_c, relative to the homogeneous fluid limit. We also explore the size of horizontal bubble velocities, affected by the damaged path.

Throughout the paper we use a Bingham model for the viscoplastic fluid. The actual yield limit is independent of the post-yield rheology for all simple yield-stress fluids where the von Mises criterion is used (i.e. Herschel–Bulkley, Bingham, Casson, etc.). However, elastic effects are present in flow onset experiments, as in Daneshi & Frigaard (2024), and EVP model formulations are now more readily available (Moschopoulos *et al.* 2021; Esposito, Dimakopoulos & Tsamopoulos 2025). Our reason for avoiding these models is twofold. Firstly, popular models such as that of Saramito (2007, 2009) are built around a description of viscoelastic flow, rather than elastic deformation and yielding. Secondly, the onset problem for an EVP fluid is not well defined. As found in Daneshi & Frigaard (2024), an initial bubble shape deforms elastically and significantly before eventually yielding plastically and flowing. The sensitivity of the deformation path to the initial bubble shape and the timeframe allowed for elastic deformation are two additional variables, not understood. Simple yield-stress fluids have a clear well-defined limit Y_c for each shape. The computed (inelastic) Y_c is likely a lower bound for associated EVP fluids, with small elastic effects, but a general theory is lacking.

2. Problem statement

We explore the yield limit of a bubble rising in a non-uniform viscoplastic fluid domain. The scenario considered is that a narrow vertical region close to the bubble has been damaged by the motion of a previous bubble. The aim is to quantify the influence of the damaged path on flow onset in a simplified model setting, so that insights can be gained regarding the industrially relevant flows described in § 1.

Our model problem uses three simplifying assumptions. First, the yield-stress fluid is modelled as a Bingham fluid, discussed above. Second, the damaged path is modelled as a vertical Newtonian channel of width equal to the bubble diameter, embedded within the viscoplastic fluid. This represents a simplified frozen heterogeneity approximation of the weakened fluid structure created by previous bubble motion. The model isolates the mechanical influence of a pre-existing pathway rather than attempting to simulate the rheological processes responsible for its formation or recovery. The choice of a Newtonian layer, as opposed to yield-stress fluid of lower yield stress is for simplicity. Lastly, we adopt a 2-D planar model, which speeds computation. An axisymmetric bubble with damaged layer would imply a damaged cylinder around the bubble, which is not representative. Hence, an expensive fully three-dimensional (3-D) computation would be the next most complete model, which is beyond the scope here. A discussion of the applicability of our 2-D results is given in § 5.

The computational domain, denoted by Ω, includes the entire fluid region: the bubble X, the surrounding Newtonian layer and the bulk viscoplastic material. The outer boundary of the domain is $\partial\Omega$, and the bubble boundary is denoted by ∂X (see figure 1). The bubble

https://doi.org/10.1017/jfm.2026.11637 Published online by Cambridge University Press

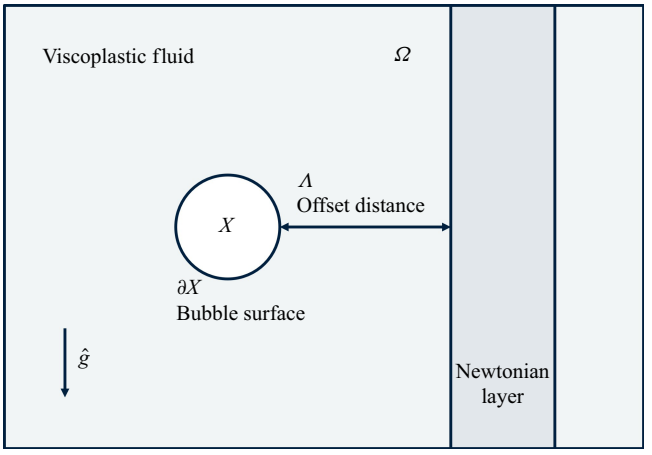


Figure 1. Schematic of the problem domain.

is assumed to have a fixed elliptical shape with aspect ratio defined as the ratio of bubble height to width: $\chi < 1$ corresponds to horizontally flattened bubbles (which we here refer to as oblate), $\chi = 1$ to circular bubbles and $\chi > 1$ to vertically elongated bubbles (which we here refer to as prolate). Here, oblate and prolate refer only to the orientation of the 2-D ellipse, and not to 3-D shapes. In all cases, due to the scaling, the area of the bubble equals π, meaning that the major and minor axes have lengths $2\sqrt{\chi}$ and $2/\sqrt{\chi}$ (or vice versa). The flow is considered in the Stokes regime, where inertia is negligible, since our questions are regarding onset of motion. We first formulate the problem in a natural way, using the buoyancy force of the bubble as the stress scale that drives the motion (mobility problem, [M]). Later we reformulate the problem as an equivalent resistance problem [R], where the bubble's mean motion is prescribed, which has some computational advantages.

2.1. *Governing equations*

The Stokes equations for the fluid region outside the bubble are

$$\boldsymbol{\nabla} \cdot \hat{\boldsymbol{\sigma}} - \hat{\rho}_f \hat{g} \boldsymbol{e}_y = 0 \quad \text{in } \Omega \setminus \overline{X}, \tag{2.1a}$$

$$\boldsymbol{\nabla} \cdot \hat{\boldsymbol{u}} = 0 \quad \text{in } \Omega \setminus \overline{X}. \tag{2.1b}$$

Here, $\hat{\boldsymbol{\sigma}}$ is the Cauchy stress tensor, $\hat{\rho}_f$ is the fluid density, $\hat{g}$ is the gravitational acceleration and $\hat{\boldsymbol{u}}$ is the fluid velocity in the domain $\Omega \setminus \overline{X}$. Dimensional quantities are denoted by the accent $\hat{\cdot}$, while non-dimensional variables appear without it. The Cauchy stress tensor is expressed as

$$\hat{\boldsymbol{\sigma}} = -\hat{p}\boldsymbol{\delta} + \hat{\boldsymbol{\tau}}, \tag{2.2}$$

where $\hat{p}$ is the pressure, $\hat{\boldsymbol{\tau}}$ is the deviatoric stress tensor and $\boldsymbol{\delta}$ is the Kronecker delta.

As we focus on the yield limit of the flow, the viscous behaviour after yielding becomes of secondary interest. Therefore, we adopt the simplest constitutive model for the viscoplastic region, the Bingham fluid model:

$$\hat{\boldsymbol{\tau}} = \begin{cases} \left(\hat{\mu}_p + \dfrac{\hat{\tau}_y}{\|\hat{\dot{\gamma}}(\hat{\boldsymbol{u}})\|}\right) \hat{\dot{\gamma}}(\hat{\boldsymbol{u}}), & \text{if } \|\hat{\tau}\| > \hat{\tau}_y, \\ \hat{\dot{\gamma}}(\hat{\boldsymbol{u}}) = 0, & \text{if } \|\hat{\tau}\| \leqslant \hat{\tau}_y, \end{cases} \tag{2.3a}$$

https://doi.org/10.1017/jfm.2026.11637 Published online by Cambridge University Press

where $\hat{\mu}_p$ is the plastic viscosity, $\hat{\tau}_y$ is the yield stress and $\hat{\dot{\gamma}}$ is the rate-of-strain tensor associated with the velocity field $\hat{\boldsymbol{u}}$. The rate-of-strain tensor is given component-wise by

$$\hat{\dot{\gamma}}_{ij}(\hat{\boldsymbol{u}}) = \frac{\partial \hat{u}_i}{\partial \hat{x}_j} + \frac{\partial \hat{u}_j}{\partial \hat{x}_i}. \tag{2.3b}$$

The appropriate norms of the rate-of-strain tensor $\hat{\dot{\gamma}}$ and deviatoric stress tensor $\hat{\boldsymbol{\tau}}$ are

$$\|\hat{\dot{\gamma}}(\hat{\boldsymbol{u}})\| = \sqrt{\frac{1}{2}\sum_{ij} \hat{\dot{\gamma}}_{ij}^2(\hat{\boldsymbol{u}})} \quad \text{and} \quad \|\hat{\tau}(\hat{\boldsymbol{u}})\| = \sqrt{\frac{1}{2}\sum_{ij} \hat{\tau}_{ij}^2(\hat{\boldsymbol{u}})}, \tag{2.3c}$$

associated with the tensor inner product $\boldsymbol{a} : \boldsymbol{b} = (1/2)\sum_{ij} a_{ij} b_{ij}$. In the damaged region, we assume the material behaves as a Newtonian fluid. The stress is linearly related to the strain rate:

$$\hat{\boldsymbol{\tau}} = \hat{\mu}_N \hat{\dot{\gamma}}(\hat{\boldsymbol{u}}), \tag{2.3d}$$

where $\hat{\mu}_N$ is the viscosity of the Newtonian fluid in the damaged region. Regarding the boundary conditions, in the far field, we specify

$$\hat{\boldsymbol{u}} = 0 \quad \text{on } \partial\Omega. \tag{2.4}$$

At the bubble surface ∂X, the fluid velocity is continuous. As the gas phase has negligible viscosity relative to the surrounding yield-stress fluid, the tangential component of stress is assumed to vanish at the surface, corresponding to a free-slip condition:

$$(\hat{\boldsymbol{\tau}} \cdot \boldsymbol{n}) \cdot \boldsymbol{t} = 0 \quad \text{on } \partial X, \tag{2.5}$$

where $\boldsymbol{n}$ and $\boldsymbol{t}$ denote the outward unit normal and tangential vectors to the bubble surface, respectively. This condition ensures that no shear stress is transmitted across the bubble boundary.

In contrast, the normal component of the stress must balance the internal gas pressure and the capillary traction due to surface tension, expressed as

$$\hat{p}_b = \hat{p} - (\hat{\boldsymbol{\tau}} \cdot \boldsymbol{n}) \cdot \boldsymbol{n} + \frac{\hat{\gamma}}{\hat{\kappa}} \quad \text{on } \partial X, \tag{2.6}$$

where $\hat{p}_b$ is the pressure inside the bubble, $\hat{\gamma}$ is the surface tension coefficient and $\hat{\kappa}$ denotes the local curvature of the interface. This relation describes the pressure jump across the bubble surface resulting from capillary forces.

2.2. *Dimensionless formulation*

2.2.1. *Mobility scaling*

To scale the problem, we select a characteristic length scale $\hat{R}$ based on the bubble radius. The characteristic velocity scale is determined by balancing the buoyancy force with viscous resistance in the viscoplastic fluids, leading to

$$\hat{U}_b = \frac{(\hat{\rho}_f - \hat{\rho}_g)\hat{g}\hat{R}^2}{\hat{\mu}_p}. \tag{2.7}$$

Stresses are scaled by the viscous stress scale $\hat{\mu}_p \hat{U}_b / \hat{R}$, which is equivalent to the buoyancy stress scale $(\hat{\rho}_f - \hat{\rho}_g)\hat{g}\hat{R}$. Using these scales, the dimensionless governing equations take the form

https://doi.org/10.1017/jfm.2026.11637 Published online by Cambridge University Press

$$\boldsymbol{\nabla}\cdot\boldsymbol{\sigma}-\frac{1}{1-\rho_r}\boldsymbol{e}_g=0,\quad \text{in } \Omega\setminus\overline{X}, \tag{2.8}$$

$$\boldsymbol{\nabla}\cdot\boldsymbol{u}=0,\quad \text{in } \Omega\setminus\overline{X}, \tag{2.9}$$

where $\rho_r=\hat{\rho}_g/\hat{\rho}_f$ is the density ratio. Since typically $\hat{\rho}_g\ll\hat{\rho}_f$, we have $\rho_r\approx 0$.

The dimensionless constitutive law for the Bingham flow is given by

$$\boldsymbol{\tau}=\begin{cases}\left(1+\dfrac{Y}{\|\dot{\boldsymbol{\gamma}}(\boldsymbol{u})\|}\right)\dot{\boldsymbol{\gamma}}(\boldsymbol{u}), & \text{iff } \|\boldsymbol{\tau}\|>Y,\\ \dot{\boldsymbol{\gamma}}(\boldsymbol{u})=0, & \text{iff } \|\boldsymbol{\tau}\|\leqslant Y,\end{cases} \tag{2.10}$$

where $Y=\hat{\tau}_y\hat{R}/\hat{\mu}_p\hat{U}_b$ is the dimensionless yield number.

For the Newtonian region, the constitutive law simplifies to

$$\boldsymbol{\tau}=\mu\dot{\boldsymbol{\gamma}}(\boldsymbol{u}), \tag{2.11}$$

where $\mu=\hat{\mu}_N/\hat{\mu}_p$ is the viscosity ratio. Generally, $\mu<1$ is assumed, implying that the damaged region is less viscous than the surrounding viscoplastic medium.

2.2.2. *Mobility variational formulation*

To derive the mobility problem [M], we first introduce $\mathcal{V}_M$ as the space of admissible velocity fields, consisting of divergence-free vector fields that vanish on the far-field boundary:

$$\mathcal{V}_M=\left\{\boldsymbol{v}:\boldsymbol{\nabla}\cdot\boldsymbol{v}=0 \text{ in } \Omega\setminus\overline{X},\quad \boldsymbol{v}=0 \text{ on } \partial\Omega\setminus\partial X\right\}. \tag{2.12}$$

Using tools from convex analysis (see e.g. Ekeland & Temam 1999), the mobility problem can be formulated as a minimisation principle. The solution velocity $\boldsymbol{u}\in\mathcal{V}_M$ is the unique minimiser of the functional

$$J_M(\boldsymbol{v})=\frac{1}{2}a(\boldsymbol{v},\boldsymbol{v})+Yj(\boldsymbol{v})-L_M(\boldsymbol{v})-T_M(\boldsymbol{v}),\qquad \boldsymbol{v}\in\mathcal{V}_M, \tag{2.13}$$

where the functionals are defined as

$$\begin{aligned}a(\boldsymbol{u},\boldsymbol{v})&=a_B(\boldsymbol{u},\boldsymbol{v})+\mu a_N(\boldsymbol{u},\boldsymbol{v}),\\&=\int_{\Omega_B}\dot{\gamma}(\boldsymbol{u}):\dot{\gamma}(\boldsymbol{v})\,\mathrm{d}\boldsymbol{\Omega}+\mu\int_{\Omega_N}\dot{\gamma}(\boldsymbol{u}):\dot{\gamma}(\boldsymbol{v})\,\mathrm{d}\boldsymbol{\Omega},\end{aligned} \tag{2.14a}$$

$$j(\boldsymbol{v})=\int_{\Omega_B}\|\dot{\gamma}(\boldsymbol{v})\|\,\mathrm{d}\boldsymbol{\Omega}, \tag{2.14b}$$

$$L_M(\boldsymbol{v})=-\frac{1}{1-\rho_r}\int_{\Omega\setminus\overline{X}}\boldsymbol{v}\cdot\boldsymbol{e}_g\,\mathrm{d}\boldsymbol{\Omega}, \tag{2.14c}$$

$$T_M(\boldsymbol{v})=-\int_{\partial X}\frac{\gamma_M}{\kappa}\boldsymbol{v}\cdot\boldsymbol{n}_j\,\mathrm{d}s. \tag{2.14d}$$

We have denoted the Bingham fluid domain by Ω_B and the Newtonian damaged layer by Ω_N, where $\Omega\setminus\overline{X}=\Omega_B\cup\Omega_N$. The functionals $a(v,v)$ and $j(v)$ represent the effects of viscous and plastic dissipation within the fluid, respectively, whereas $L_M(v)$ and $T_M(v)$ correspond to the work done by buoyancy and surface tension. The surface tension term is

https://doi.org/10.1017/jfm.2026.11637 Published online by Cambridge University Press

also scaled with the characteristic buoyancy stress, so that

$$\gamma_M = \frac{\hat{\gamma}}{(\hat{\rho}_f - \hat{\rho}_g)\hat{g}\hat{R}^2}. \tag{2.15}$$

A dual variational principle can also be formulated in terms of the admissible stress tensor $\tilde{\boldsymbol{\tau}}$. If $\boldsymbol{u}$ is the minimiser of J_M, then the corresponding stress field $\boldsymbol{\tau}$ maximises the functional

$$I(\tilde{\boldsymbol{\tau}}) = \frac{1}{2}\int_{\Omega\setminus\overline{X}} \left(\|\tilde{\boldsymbol{\tau}}\| - Y\right)_+^2 \,\mathrm{d}\Omega, \tag{2.16}$$

where $(\cdot)_+$ denotes the positive part.

Generally, the primal and dual problems are linked through the following inequalities (originally derived by Prager (1954) for simpler flows):

$$I(\tilde{\boldsymbol{\tau}}) \leqslant I(\boldsymbol{\tau}) = J_M(\boldsymbol{u}) \leqslant J_M(\boldsymbol{v}). \tag{2.17}$$

Thus, the velocity solution $\boldsymbol{u}$ uniquely minimises J_M over the admissible space $\mathcal{V}_M$, while the associated stress field $\boldsymbol{\tau}$ maximises I. For the exact solution, the difference between these two functionals vanishes, whereas for approximate admissible fields it remains strictly positive, known as the duality gap.

Most computational methods are based on solving the velocity minimisation. This may be equivalently formulated as a variational inequality, i.e. $\boldsymbol{u} \in \mathcal{V}_M$ satisfies

$$a(\boldsymbol{u}, \boldsymbol{v} - \boldsymbol{u}) + Y[j(\boldsymbol{v}) - j(\boldsymbol{u})] \geqslant L_M(\boldsymbol{v} - \boldsymbol{u}) + T_M(\boldsymbol{v} - \boldsymbol{u}), \quad \forall \boldsymbol{v} \in \mathcal{V}_M. \tag{2.18}$$

Lastly, the solution $\boldsymbol{u} \in \mathcal{V}_M$ satisfies the steady (mechanical) energy equation:

$$a(\boldsymbol{u}, \boldsymbol{u}) + Yj(\boldsymbol{u}) = L_M(\boldsymbol{u}) + T_M(\boldsymbol{u}), \tag{2.19}$$

which is used in defining the yield limit.

2.2.3. *Resistance scaling and formulation*

In dealing with particle settling problems, a resistance formulation is often adopted, i.e. the particle motion is imposed and the resisting force calculated. This formulation is less natural for bubbles and droplets that may deform while moving. Indeed unlike rigid particles, where the velocity can be imposed directly on the boundary ∂X as in Putz & Frigaard (2010), the bubble surface velocity is not easily determined. However, we shall see later that the resistance formulation has advantages in determining flow onset for specified interface shapes, where deformation of the interface with time is not a concern, i.e. because we determine a static limit.

For the resistance formulation [R] we use the vertical component of the mean bubble velocity $\hat{U}_0$, as velocity scale. Since the velocity field is divergence-free, the net volumetric flux across the entire domain Ω must be zero. Thus, the downward flux of the fluid domain must balance the upward motion of the bubble. This constraint allows us to express the mean bubble velocity in terms of the fluid velocity field:

$$\hat{U}_0 = -\frac{1}{\pi\hat{R}^2}\int_{\Omega\setminus\overline{X}} \hat{\boldsymbol{u}} \cdot \boldsymbol{e}_g \,\mathrm{d}\Omega. \tag{2.20}$$

https://doi.org/10.1017/jfm.2026.11637 Published online by Cambridge University Press

On scaling velocities with $\hat{U}_0$ and lengths with $\hat{R}$, we see that the dimensionless velocity $\boldsymbol{u}^*$ lies in the set $\mathcal{V}_R$ of admissible velocity fields:

$$\mathcal{V}_R = \left\{ \boldsymbol{v}^* : \int_{\Omega\setminus\overline{X}} \boldsymbol{v}^* \cdot \boldsymbol{e}_g \, \mathrm{d}\Omega = -\pi; \;\; \boldsymbol{\nabla}\cdot\boldsymbol{v}^* = 0, \;\; \text{in } \Omega\setminus\overline{X}; \;\; \boldsymbol{v}^* = 0 \text{ on } \partial\Omega \right\}. \tag{2.21}$$

The solution $\boldsymbol{u}^* \in \mathcal{V}_R$ is the minimiser of

$$J_R(\boldsymbol{v}^*) = \frac{1}{2} a(\boldsymbol{v}^*, \boldsymbol{v}^*) + Bj(\boldsymbol{v}^*) - L_R(\boldsymbol{v}^*) - T_R(\boldsymbol{v}^*), \quad \boldsymbol{v}^* \in \mathcal{V}_R, \tag{2.22}$$

where the linear functionals $L_R(\boldsymbol{v}^*)$ and $T_R(\boldsymbol{v}^*)$ represent the effects of buoyancy and surface tension, respectively:

$$L_R(\boldsymbol{v}^*) = -\frac{1}{1-\rho_r}\frac{B}{Y}\int_{\Omega\setminus\overline{X}} \boldsymbol{e}_g \cdot \boldsymbol{v}^* \, \mathrm{d}\Omega, \tag{2.23a}$$

$$T_R(\boldsymbol{v}^*) = -\int_{\partial X} \frac{\gamma_R}{\kappa} \boldsymbol{v}^* \cdot \boldsymbol{n} \, \mathrm{d}S. \tag{2.23b}$$

Here, the non-dimensional Bingham number B and surface tension parameter γ_R are defined as

$$B = \frac{\hat{\tau}_y \hat{R}}{\hat{\mu}\hat{U}_0}, \tag{2.24}$$

$$\gamma_R = \frac{\hat{\gamma}}{\hat{\mu}\hat{U}_0}. \tag{2.25}$$

As with the mobility formulation, the velocity minimisation can be written as a variational inequality. The mechanical energy balance in the resistance formulation is given by

$$a(\boldsymbol{u}^*, \boldsymbol{u}^*) + Bj(\boldsymbol{u}^*) = L_R(\boldsymbol{u}^*) + T_R(\boldsymbol{u}^*), \tag{2.26}$$

for the solution $\boldsymbol{u}^* \in \mathcal{V}_R$.

2.3. *Mapping between mobility and resistance formulations*

The two formulations introduced differ in their choice of velocity scale. While the mobility formulation leads to an easier computational implementation, we will see below that the yield limit is defined by the ratio of two functionals that both approach zero in this limit. The resistance formulation avoids this feature. Thus, although we have used both formulations for computation, the resistance formulation has some advantage in computing the yield limit. The relationship between the Bingham number B and the yield number Y is reflected in the ratio of the characteristic velocities used in each formulation:

$$\frac{B}{Y} = \frac{\hat{U}_b}{\hat{U}_0}. \tag{2.27}$$

Note that since the yield limit is defined by a stationary bubble, $\hat{U}_0 = 0$, we see that $B \to \infty$ at flow onset.

To express the resistance formulation in terms of the mobility variables, we apply the scaling $\boldsymbol{u}^* = (\hat{U}_b/\hat{U}_0)\boldsymbol{u}$, where $\boldsymbol{u}^* \in \mathcal{V}_R$ and $\boldsymbol{u} \in \mathcal{V}_M$. Using (2.27) and

$$\gamma_R = \frac{B}{Y}\gamma_M, \tag{2.28}$$

https://doi.org/10.1017/jfm.2026.11637 Published online by Cambridge University Press

we see that the energy equation in the resistance formulation is

$$a(\boldsymbol{u}^*, \boldsymbol{u}^*) + Bj(\boldsymbol{u}^*) = \frac{B}{Y}[L_M(\boldsymbol{u}^*) + T_M(\boldsymbol{u}^*)], \tag{2.29}$$

$$\left(\frac{B}{Y}\right)^2 a(\boldsymbol{u}, \boldsymbol{u}) + B\left(\frac{B}{Y}\right) j(\boldsymbol{u}) = \left(\frac{B}{Y}\right)^2 [L_M(\boldsymbol{u}) + T_M(\boldsymbol{u})], \tag{2.30}$$

which is (2.19).

2.4. *Yield limit calculation*

The yield limit of bubble motion is the conditions under which a bubble ceases to move in a viscoplastic fluid. This happens when Y exceeds a critical value Y_c, and the material does not yield anywhere. Using the variational framework introduced earlier, following Dubash & Frigaard (2004), assuming that $\boldsymbol{u} \neq 0$:

$$\begin{aligned} 0 \leqslant a(\boldsymbol{u}, \boldsymbol{u}) = L_M(\boldsymbol{u}) + T_M(\boldsymbol{u}) - Yj(\boldsymbol{u}) &= j(\boldsymbol{u})\left[\frac{L_M(\boldsymbol{u}) + T_M(\boldsymbol{u})}{j(\boldsymbol{u})} - Y\right] \\ &\leqslant j(\boldsymbol{u})\left[\sup_{\boldsymbol{v}\in\mathcal{V}_M,\, \boldsymbol{v}\neq 0} \frac{L_M(\boldsymbol{v}) + T_M(\boldsymbol{v})}{j(\boldsymbol{v})} - Y\right] = j(\boldsymbol{u})[Y_c - Y], \end{aligned} \tag{2.31}$$

where Y_c is defined by

$$Y_c = \sup_{\boldsymbol{v}\in\mathcal{V}_M,\, \boldsymbol{v}\neq 0} \frac{L_M(\boldsymbol{v}) + T_M(\boldsymbol{v})}{j(\boldsymbol{v})}. \tag{2.32}$$

Having found Y_c, in the limit $Y \to Y_c^-$, it can be shown that

$$a(\boldsymbol{u}, \boldsymbol{u}) = \mathcal{O}\left((Y_c - Y)^2\right), \tag{2.33a}$$

$$j(\boldsymbol{u}) = \mathcal{O}(Y_c - Y), \tag{2.33b}$$

and also that the viscous dissipation $a(\boldsymbol{u}, \boldsymbol{u})$ decays at least one order of magnitude faster than the plastic dissipation term $j(\boldsymbol{u})$.

Since (2.32) appears daunting to evaluate, an alternative is a simple and direct method of calculation, i.e. increase Y from zero until the solution decays to zero, as (2.33) guarantees. Figure 2 shows the typical decay of these functionals as Y_c is approached from below, computed using formulation [M] for two examples with an oblate bubble.

For each functional f we have fitted a power-law model to the last four points calculated, using MATLAB's `polyfit` applied to the log–log data of f versus $(1 - Y/Y_c)$. The resulting exponents and prefactors are reported in table 1. We have separately calculated the viscous dissipation into contributions from the Bingham and Newtonian domains, $a_B(\boldsymbol{u}, \boldsymbol{u})$ and $a_N(\boldsymbol{u}, \boldsymbol{u})$, respectively. These display the expected faster decay, with exponents close to 2, while the plastic dissipation $j_B(\boldsymbol{u})$, the buoyancy work $L_M(\boldsymbol{u})$ and the surface tension work $T_M(\boldsymbol{u})$ all decay at comparable rates closer to unity. This decay is consistent with the theoretical decay described in (2.33): $a(\boldsymbol{u}, \boldsymbol{u}) = O((Y_c - Y)^2)$ and $j(\boldsymbol{u}) = O(Y_c - Y)$, confirming that the numerical results capture the correct limiting behaviour as $Y \to Y_c^-$.

The computed solutions used for the values plotted in figure 2 were calculated from the mobility formulation [M], using the code developed for Pourzahedi *et al.* (2022). Since we are concerned primarily with the limit of zero flow, this code uses an AL framework, originally introduced by Glowinski, Lions & Tremolieres (1981), which computes unyielded regions of fluid as having zero strain rate. The computations are

https://doi.org/10.1017/jfm.2026.11637 Published online by Cambridge University Press

Functional	$\gamma_M = 0$		$\gamma_M = 1$	
	p	C	p	C
$a_N(\boldsymbol{u}, \boldsymbol{u})$	2.2661	0.0030	1.5501	0.0000
$a_B(\boldsymbol{u}, \boldsymbol{u})$	2.0570	0.4317	1.4717	0.0391
$j_B(\boldsymbol{u})$	1.1413	3.0342	0.7844	0.3744
$L_M(\boldsymbol{u})$	1.1396	0.6606	0.7862	0.0406
$T_M(\boldsymbol{u})$	—	—	0.7826	0.1023

Table 1. Power-law fits $f \sim C\, x^p$ for the functionals under $\gamma_M = 0$ and $\gamma_M = 1$.

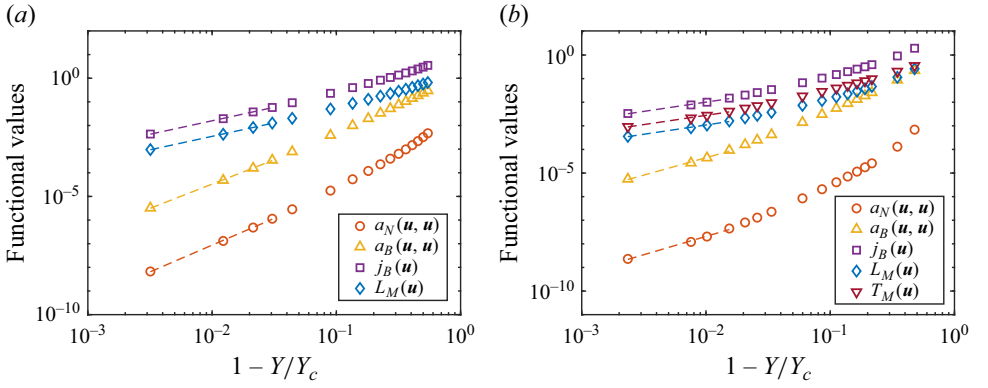


Figure 2. Computed decay of the energy functionals as $Y \to Y_c^-$ for an oblate bubble $\chi = 0.5$ positioned at $\Lambda = 1$. The viscosity ratio is fixed at $\mu = 0.001$ for all computations shown (unless stated otherwise): (*a*) $\gamma_M = 0$, $Y_c = 0.2197$; (*b*) $\gamma_M = 1$, $Y_c = 0.3829$. Functionals plotted are: $a_N(\boldsymbol{u}, \boldsymbol{u})$ (Newtonian viscous dissipation), $a_B(\boldsymbol{u}, \boldsymbol{u})$ (Bingham dissipation), $j(\boldsymbol{u})$ (plastic dissipation), $L_M(\boldsymbol{u})$ (buoyancy work) and $T_M(\boldsymbol{u})$ (surface tension work). The dashed lines show the power-law fits obtained from the last four data points using MATLAB's `polyfit`.

implemented in `FreeFEM++` (Hecht 2012), with adaptive triangular mesh refinement near yield surfaces. The finite-element discretisation follows standard practices, using mixed Taylor–Hood elements for velocity and pressure, consistent with the approaches pioneered in Roquet & Saramito (2003).

The fitting procedure captured in table 1 is of course sensitive to the value of Y_c used. Directly calculating Y_c leads to some ambiguity, e.g. which functional should one monitor to evaluate whether $\boldsymbol{u} = 0$: $L_M(\boldsymbol{u})$, $T_M(\boldsymbol{u})$ or $j(\boldsymbol{u})$? Since the numerical method is also iterating to a specified tolerance at the same time as the solution becomes close to zero, there are further difficulties in accurately stating the value of Y at which the flow has stopped. Therefore, a new method is needed to identify Y_c.

As argued elsewhere (Putz & Frigaard 2010; Chaparian & Frigaard 2017), the redundancy of the viscous dissipation terms in the $Y \to Y_c^-$ limit suggests that the solution $\boldsymbol{u} = \boldsymbol{u}(Y)$ is itself a minimiser of (2.32) in the limit $Y \to Y_c^-$. On rearranging (2.19), we find

$$Y = \frac{L_M(\boldsymbol{u}) + T_M(\boldsymbol{u})}{j(\boldsymbol{u})} - \frac{a(\boldsymbol{u}, \boldsymbol{u})}{j(\boldsymbol{u})}, \quad \boldsymbol{u}(Y) \neq 0, \tag{2.34}$$

$$Y_c = \lim_{Y \to Y_c^-} \left\{ \frac{L_M(\boldsymbol{u}) + T_M(\boldsymbol{u})}{j(\boldsymbol{u})} \right\} + \mathcal{O}(Y_c - Y). \tag{2.35}$$

https://doi.org/10.1017/jfm.2026.11637 Published online by Cambridge University Press

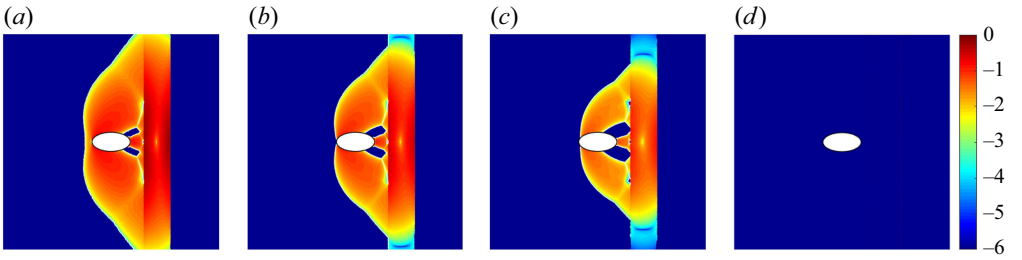


Figure 3. Formulation [M] strain rate contours ($\log \|\dot{\boldsymbol{\gamma}}\|$) plotted for an oblate bubble $\chi = 0.5$ positioned at $\Lambda = 1$ with $\gamma_M = 0$, shown for four values of the yield number: (*a*) $Y = 0.13$, (*b*) $Y = 0.16$, (*c*) $Y = 0.19$ and (*d*) $Y = 0.22$.

Therefore, the limiting solutions may be used to evaluate Y_c. As seen in figure 2 and as follows theoretically from (2.34), the plastic dissipation term $j(\boldsymbol{u})$ dominates over the viscous dissipation $a(\boldsymbol{u}, \boldsymbol{u})$ in this limit. It may appear that we have improved on the direct method, by evaluating Y_c as the ratio in (2.35). However, since both numerator and denominator vanish, (2.35) leads to an indeterminate limit. This is further illustrated in figure 3, which plots the strain-rate fields obtained from the mobility formulation for several values of $Y < Y_c$, corresponding to the progression in figure 2. The sequence highlights the transition from yielded bubble flow to a near-rigid plug as $Y \to Y_c^-$.

3. Computing solutions and yield limits using the resistance formulation

We have seen that the mobility formulation has some limitations for finding the yield limit. Firstly, there is naturally a problem in distinguishing zero velocity from iterating to a numerically small tolerance. Secondly, as discussed above, (2.35) becomes indeterminate as the flow stops. Therefore, we switch from mobility to resistance formulation in order to be able to compute the yield limit robustly.

3.1. *An AL approach*

This section may be skipped for the reader uninterested in detail of the method used. The chief difficulty with the [R] formulation is in ensuring the bubble rise constraint: unlike a solid particle, only the mean motion is enforced. The AL functional used for the resistance formulation is

$$\begin{aligned}\mathcal{L}(\boldsymbol{v}^*, \boldsymbol{q}, \boldsymbol{\lambda}, k) = \frac{1}{2}a(\boldsymbol{q}, \boldsymbol{q}) + Bj(\boldsymbol{q}) + L_R(\boldsymbol{v}^*) + T_R\left(\boldsymbol{v}^*\right) \\ + \frac{r}{2}\int_{\Omega\setminus\overline{X}} \left(\boldsymbol{q} - \dot{\boldsymbol{\gamma}}\left(\boldsymbol{v}^*\right)\right)^2 \,\mathrm{d}\Omega \\ + \int_{\Omega\setminus\overline{X}} \boldsymbol{\lambda}\cdot\left(\boldsymbol{q} - \dot{\boldsymbol{\gamma}}\left(\boldsymbol{v}^*\right)\right) \,\mathrm{d}\Omega \\ + \int_{\Omega\setminus\overline{X}} k\left(v_y^* + \pi\right) \,\mathrm{d}\Omega. \end{aligned} \tag{3.1}$$

Here $\boldsymbol{v}^* \in \mathcal{V}_R$ is an admissible velocity and $\boldsymbol{q}$ is an auxiliary strain-rate tensor variable. There are two Lagrange multipliers: $\boldsymbol{\lambda}$ is a tensor that enforces the constitutive law and k is a scalar that is used to enforce the flux constraint, needed for the solution to be in $\mathcal{V}_R$. We solve a saddle-point problem for $\mathcal{L}(\boldsymbol{v}^*, \boldsymbol{q}, \boldsymbol{\lambda}, k)$, using an iterative Uzawa algorithm.

https://doi.org/10.1017/jfm.2026.11637 Published online by Cambridge University Press

At convergence, we expect

$$\boldsymbol{q} \to \dot{\boldsymbol{\gamma}}(\boldsymbol{v}^*), \quad \boldsymbol{\lambda} \to \boldsymbol{\tau}^*, \quad \int_{\Omega \setminus \overline{X}} v_y^* \, \mathrm{d}\Omega \to -\pi. \tag{3.2}$$

Much of the algorithm is standard for those familiar with AL methods. We solve sequentially for optimality of $\boldsymbol{v}^*$, $\boldsymbol{q}$ and $\boldsymbol{\lambda}$, and then iteratively. The main difference comes in solving for the optimal $\boldsymbol{v}^*$, wherein we also update k automatically.

At the beginning of the solution procedure, we compute a homogeneous base flow solution $(\boldsymbol{u}_H^*, p_H^*)(k)$, which corresponds to a unit buoyancy force. This is the solution of

$$-\boldsymbol{\nabla} p_H^* + \boldsymbol{\nabla} \cdot [r\dot{\boldsymbol{\gamma}}(\boldsymbol{u}_H^*)] = \left(k + \frac{B}{Y}\right) \boldsymbol{e}_y \quad \text{in } \Omega \setminus \overline{X}, \tag{3.3}$$

$$\boldsymbol{\nabla} \cdot \boldsymbol{u}_H^* = 0 \quad \text{in } \Omega \setminus \overline{X}, \tag{3.4}$$

$$\boldsymbol{u}_H^* = \boldsymbol{0} \quad \text{on } \partial\Omega. \tag{3.5}$$

The unit vector in the vertical direction is $\boldsymbol{e}_y$. The following interface conditions are satisfied on ∂X:

$$p_H^* - r\dot{\gamma}_{nn}(\boldsymbol{u}_H^*) = \text{const.}, \tag{3.6}$$

$$r\dot{\gamma}_{nt}(\boldsymbol{u}_H^*) = 0. \tag{3.7}$$

If $k = k_0 \equiv 1 - (B/Y)$, then a unit buoyancy force pushes the fluid downwards (in response to the bubble rising). The vertical areal flux due to $\boldsymbol{u}_H^*(k)$ is

$$Q(k) = \int_{\Omega \setminus \overline{X}} (\boldsymbol{u}_H^*)_y(k) \, \mathrm{d}\Omega. \tag{3.8}$$

Due to linearity, we see that $(\boldsymbol{u}_H^*, p_H^*)(k) = (k + B/Y)(\boldsymbol{u}_H^*, p_H^*)(k_0)$, which is the homogeneous base flow solution driven by buoyancy force $(k + B/Y)$, and evidently has vertical areal flux $Q(k) = (k + B/Y)Q(k_0)$.

3.1.1. *Velocity iteration*

Suppose that $(\boldsymbol{q}, \boldsymbol{\lambda}) = (\boldsymbol{q}^{n-1}, \boldsymbol{\lambda}^{n-1})$ are known at step $n-1$. At iteration n, the optimality conditions on $\boldsymbol{v}^* \in \mathcal{V}_R$ define the velocity problem, the solution of which is $\boldsymbol{u}^*$ $(= \boldsymbol{u}^{*,n})$. Below we suppress the iteration superscript, for simplicity of notation. We decompose the velocity $\boldsymbol{u}^*$ into two parts:

$$\boldsymbol{u}^* = \boldsymbol{u}_H^* + \boldsymbol{u}_N^*. \tag{3.9}$$

Here $\boldsymbol{u}_H^*$ represents a buoyancy-driven base flow and $\boldsymbol{u}_N^*$ is a correction that enforces the viscoplastic constitutive law as it converges. Since the optimality conditions on $\boldsymbol{v}^*$ result in a linear problem for $\boldsymbol{u}^*$, two linear problems can be separately defined for $\boldsymbol{u}_H^*$ and $\boldsymbol{u}_N^*$, then joined by superposition.

The correction $(\boldsymbol{u}_N^*, p_N^*)$ is found at each iteration as the solution of

$$-\boldsymbol{\nabla} p_N^* + \boldsymbol{\nabla} \cdot [r\dot{\boldsymbol{\gamma}}(\boldsymbol{u}_N^*)] + \boldsymbol{\nabla} \cdot (\boldsymbol{\lambda} - r\boldsymbol{q}) = \boldsymbol{0} \quad \text{in } \Omega \setminus \overline{X}, \tag{3.10}$$

$$\boldsymbol{\nabla} \cdot \boldsymbol{u}_N^* = 0 \quad \text{in } \Omega \setminus \overline{X}, \tag{3.11}$$

$$\boldsymbol{u}_N^* = \boldsymbol{0} \quad \text{on } \partial\Omega, \tag{3.12}$$

with interface conditions on ∂X:

$$p_N^* - r(\dot{\gamma}_{nn}(\boldsymbol{u}_N^*) - q_{nn}) - \lambda_{nn} + \frac{B}{Y}\gamma = \text{const.}, \tag{3.13}$$

$$-r(\dot{\gamma}_{nt}(\boldsymbol{u}_N^*) - q_{nt}) - \lambda_{nt} = 0. \tag{3.14}$$

https://doi.org/10.1017/jfm.2026.11637 Published online by Cambridge University Press

Having solved for $(\boldsymbol{u}_N^*,\, p_N^*)$, we compute the vertical areal flux:

$$Q_N = \int_{\Omega\setminus\overline{X}} u_{N,y}^*\,\mathrm{d}\Omega. \tag{3.15}$$

We now determine $k\,(=k^n)$ by the requirement that $\boldsymbol{u}^* = \boldsymbol{u}_H^*(k) + \boldsymbol{u}_N^* \in \mathcal{V}_R$:

$$\begin{aligned} -\pi = Q_N + Q(k) = Q_N + (k + B/Y)Q(k_0) \implies \\ k = -\frac{B}{Y} - \frac{\pi + Q_N}{Q(k_0)} = k_0 - \frac{\pi + Q_N + Q(k_0)}{Q(k_0)}. \end{aligned} \tag{3.16}$$

3.1.2. *Uzawa-based resistance algorithm*

The overall algorithm proceeds as follows. We initialise $n = 0$, and set the initial guesses $\boldsymbol{q}^0$ and $\boldsymbol{\lambda}^0$, typically both set to zero. We compute $(\boldsymbol{u}_H^*,\, p_H^*)(k_0)$ to initialise. On iteration $n \geqslant 1$ we sequentially perform the following steps.

(i) Using $(\boldsymbol{q}^{n-1},\, \boldsymbol{\lambda}^{n-1})$, compute $(\boldsymbol{u}^*)^n = \boldsymbol{u}_H^* + \boldsymbol{u}_N^*$ and k^n as described in § 3.1.1.

(ii) Update the plastic strain rate, $\boldsymbol{q}^n$, according to

$$\boldsymbol{q}^n = \left(1 - \frac{B(\boldsymbol{x})}{\left\|\boldsymbol{\lambda}^{n-1} + r\mu(\boldsymbol{x})\dot{\boldsymbol{\gamma}}((\boldsymbol{u}^*)^{n+1})\right\|}\right)_+ \frac{\boldsymbol{\lambda}^{n-1} + r\mu(\boldsymbol{x})\dot{\boldsymbol{\gamma}}((\boldsymbol{u}^*)^{n+1})}{\mu(\boldsymbol{x})(1+r)}, \tag{3.17}$$

where $B(\boldsymbol{x}) = 0$ in the weakened Newtonian layer and $B(\boldsymbol{x}) = B$ in the Bingham fluid. Similarly, $\mu(\boldsymbol{x}) = 1$ in Ω_B and $\mu(\boldsymbol{x}) = \mu$ in Ω_N.

(iii) Update the Lagrange multiplier $\boldsymbol{\lambda}^n$:

$$\boldsymbol{\lambda}^n = \boldsymbol{\lambda}^{n-1} + r\mu(\boldsymbol{x})\left[(\dot{\boldsymbol{\gamma}}((\boldsymbol{u}^*)^n) - \boldsymbol{q}^n\right]. \tag{3.18}$$

Convergence is monitored through

$$\max\left\{\left\|\boldsymbol{u}^{*,n} - \boldsymbol{u}^{*,n-1}\right\|_{L^2},\ \left\|\boldsymbol{q}^{\,n} - \boldsymbol{q}^{\,n-1}\right\|_{L^2},\ \left\|\boldsymbol{q}^{\,n} - \dot{\boldsymbol{\gamma}}((\boldsymbol{u}^*)^n)\right\|_{L^2}\right\}. \tag{3.19}$$

3.2. *Benchmark problems*

To benchmark the numerical implementation of the resistance formulation, we reproduce and compare results for a single bubble in a uniform medium using the mobility formulation as a reference. This allows us to verify consistency between the two formulations before introducing any spatial non-uniformity. Figure 4 shows an example of this comparison. The velocity contours obtained from both the resistance and mobility formulations for an oblate bubble ($\chi = 0.5$) are plotted with surface tension parameter $\gamma_M = 1$. The two solutions coincide, with the only difference being that the resistance formulation results are scaled such that the mean bubble rise velocity is 1, as noted previously.

Secondly, figure 5 shows the decay of the duality gap, with successive iterations in both mobility and resistance algorithms. As discussed in Treskatis *et al.* (2018), the duality gap provides the most reliable measure for assessing the accuracy of both stress and velocity fields, particularly in computations close to the yield point.

https://doi.org/10.1017/jfm.2026.11637 Published online by Cambridge University Press

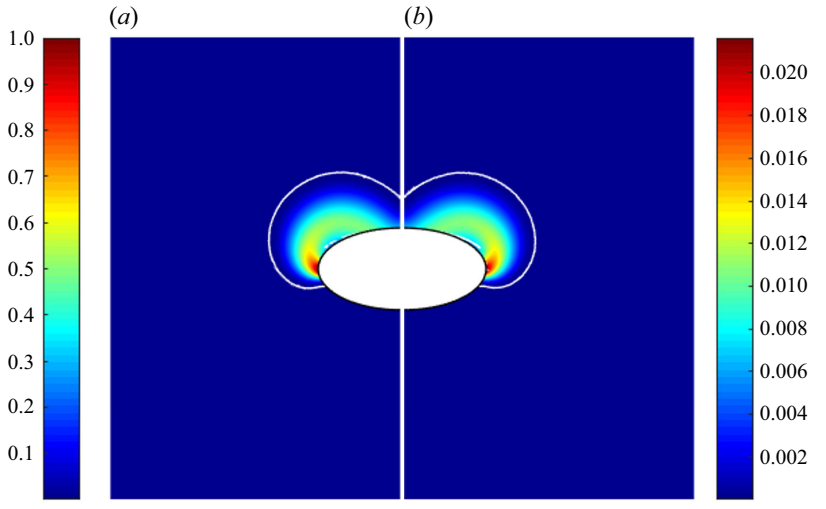


Figure 4. The magnitude of velocity fields around an elliptical bubble for $\chi = 0.5$ with $\gamma_M = 1$: (*a*) results from the [R] problem at $B = 100$ and (*b*) results from the [M] problem with an equivalent yield number $Y = 0.277$ (Pourzahedi *et al.* 2022). White lines indicate the yield surfaces separating yielded and unyielded regions.

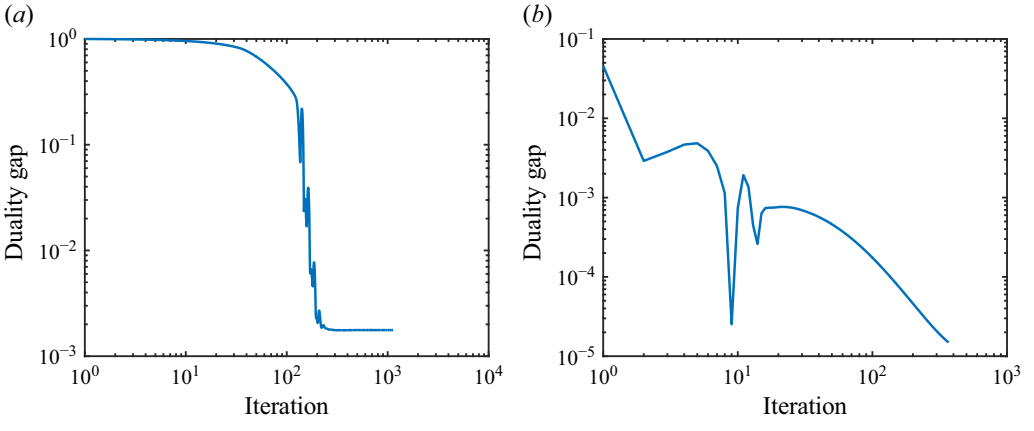


Figure 5. Convergence of the duality gap for (*a*) the [R] problem and (*b*) the [M] problem. The computations are carried out for parameters equivalent to those of figure 4.

3.3. *Evaluating* Y_c

As discussed in § 2.4, the reason for adopting the resistance formulation is to avoid the indeterminate limit in (2.35). In the resistance formulation, we have

$$Y_c = \lim_{B\to\infty} \frac{L_R(\boldsymbol{u}^*) + T_R(\boldsymbol{u}^*)}{j(\boldsymbol{u}^*) + \dfrac{a(\boldsymbol{u}^*, \boldsymbol{u}^*)}{B}}. \tag{3.20}$$

Figure 6(*a*) demonstrates the convergence of the quotient in (3.20). Note that now we have no indeterminacy since $L_R(\boldsymbol{u}^*) = -\pi$ in the resistance formulation and there is always a strain rate local to the bubble, as the velocity changes from $O(1)$ near the bubble to 0 in the far field. In figure 6(*a*) we can see that the approximation (3.20) to Y_c is still slightly

https://doi.org/10.1017/jfm.2026.11637 Published online by Cambridge University Press

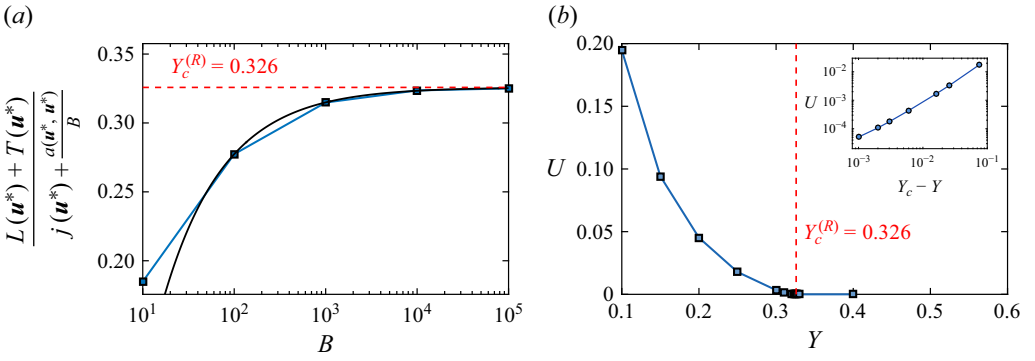


Figure 6. (*a*) Convergence of the ratio in (3.20) to Y_c for the [R] problem for a bubble with $\chi = 0.5$ and $\gamma_M = 1$. (*b*) Decay of the mean rise velocity of the same bubble with increasing Y, based on results from the [M] problem.

increasing even at $B = 10^5$. Consequently, to estimate the asymptotic value Y_c as $B \to \infty$, we fit the computed values of $Y(B)$ to

$$Y(B) = Y_c - d\, B^{-\nu}. \tag{3.21}$$

The parameters (Y_c, d, ν) are obtained by nonlinear least squares, solved using a Levenberg–Marquardt scheme, which is well suited to smooth nonlinear regressions of this type. In practice, the smallest Bingham numbers are excluded from the regression fitting, being outside the asymptotic range. This procedure yields stable and consistent estimates of $Y_c = Y_c^{[R]}$ across all configurations that we have computed. The earlier values of Y_c used, e.g. in figure 2, were obtained using this method. To assess the sensitivity of the extrapolation, the regression was repeated using different fitting windows by excluding subsets of the smallest Bingham numbers. Across all configurations considered, the resulting values of Y_c varied by less than approximately 0.15 %, indicating that the asymptotic estimate of Y_c is relatively insensitive to the choice of fitting range.

In figure 6(*b*) we plot the decay of the mean rise velocity U with increasing Y, calculated using the [M] problem, together with the limit $Y_c = Y_c^{[R]}$ determined in figure 6(*a*) as the vertical dashed line. The inset shows U plotted against $Y_c - Y$ on a log–log scale. The decay of the data as $Y \to Y_c^-$ confirms that the mobility formulation is consistent with the same limiting value of Y_c.

4. Results

Our main results concern how the critical yield number Y_c for 2-D bubble motion with a nearby damaged Newtonian layer depends on various parameters. Most of the results are obtained from simulations of the resistance problem, for which Y_c is estimated from the asymptotic behaviour at large Bingham numbers of the ratio in (3.20). We explore the effects of the offset distance Λ (§ 4.1), the bubble aspect ratio χ (§ 4.2), the surface tension parameter γ_M (§ 4.3) and the viscosity ratio μ (§ 4.4). Lastly, we assess the effects of the damaged layer on lateral motion of the bubble (§ 4.5).

4.1. *Offset distance effect on onset of motion*

First, we examine how the critical yield number Y_c depends on the offset distance Λ between the bubble and the Newtonian layer, as defined in figure 1. Note that we use the

https://doi.org/10.1017/jfm.2026.11637 Published online by Cambridge University Press

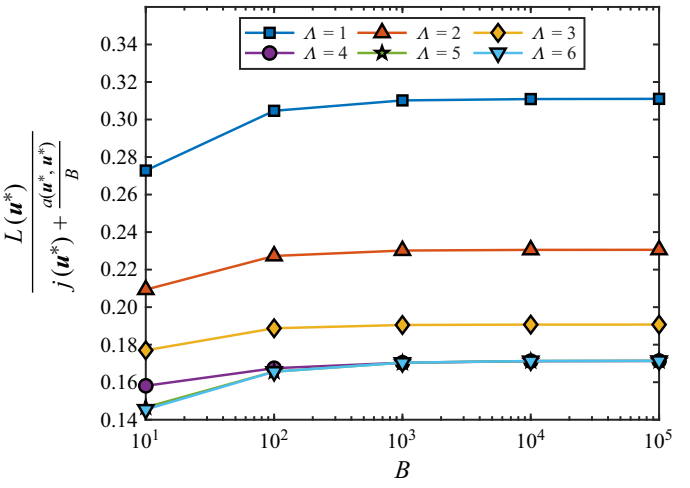


Figure 7. Convergence of computed critical yield number Y_c for a circular bubble at various offset distances from a damaged region; $\gamma_M = 0$.

edge-to-edge offset distance to define Λ, as it is less affected by bubble shape, i.e. centre-to-centre distance would be limited at small χ. Figure 7 shows results computed from the resistance-based formulation (3.20) for a circular bubble, $\chi = 1$. For small offsets ($\Lambda = 1$), we see that Y_c is significantly elevated compared with the case of a uniform viscoplastic fluid, with no Newtonian layer. In other words, a larger yield stress is needed in order to keep the bubble static when it lies close to the Newtonian layer.

In this regime of elevated Y_c, the stress field generated by the bubble rise, which yields the fluid within an envelope before and after the bubble, is less confined. The yielded envelope connects to the Newtonian layer, allowing the bubble to move. As Λ increases, the extent of this overlap in stress fields diminishes and the effect of the Newtonian layer weakens, leading to a gradual decrease in Y_c. Beyond a critical offset ($\Lambda \approx 4$), the Newtonian layer lies entirely outside the stress-bearing zone, and Y_c converges to a plateau of approximately $Y_c \approx 0.171$, consistent with the value reported for a uniform viscoplastic medium (Pourzahedi *et al.* 2022). As seen in figure 7, all the limiting curves of (3.20) overlap at large B. Although the $\Lambda = \infty$ value for Y is recovered, it is worth noting that $\Lambda_c \approx 4$ is significantly larger than the radius of the yielded envelope around the single bubble in an unyielded medium (see Pourzahedi *et al.* 2022). The stresses do not vanish at the yielded envelope boundary, but continue to vary within the unyielded fluid, and hence are influenced at greater distances. Similar sensitivity, through the stress field at distances greater than the yielded envelope distance, is found in the study of multiple particles settling in yield stress fluids (Liu, Muller & Denn 2003; Chaparian, Wachs & Frigaard 2018).

Although the resistance method provides a robust way of evaluating (3.20), it is worth noting that extrapolating to the limit at $B \to \infty$ is still needed. Here the procedure used is that described in § 3.3, i.e. fitting to the expression in (3.21). The resulting asymptotic values are reported in table 2. The alternative to this fitting procedure could be to compute at larger B. The range of Bingham numbers considered is, however, still limited by computational constraints, but different from those of problem [M]. In problem [R], computational challenges at high Bingham numbers arise due to the growth of unyielded plug regions as B increases. The unyielded regions expand while the surrounding yielded (sheared) layers become progressively thinner in parts. The thin layers need increasingly

https://doi.org/10.1017/jfm.2026.11637 Published online by Cambridge University Press

Λ	Y_c	d	ν
1	0.3110	0.3629	0.8773
2	0.2306	0.2270	0.9205
3	0.1907	0.1490	0.9397
4	0.1714	0.06035	0.5909
5	0.1714	0.1863	0.7526
6	0.1715	0.1850	0.7505

Table 2. Asymptotic fit parameters Y_c, d and ν for $\chi = 1$.

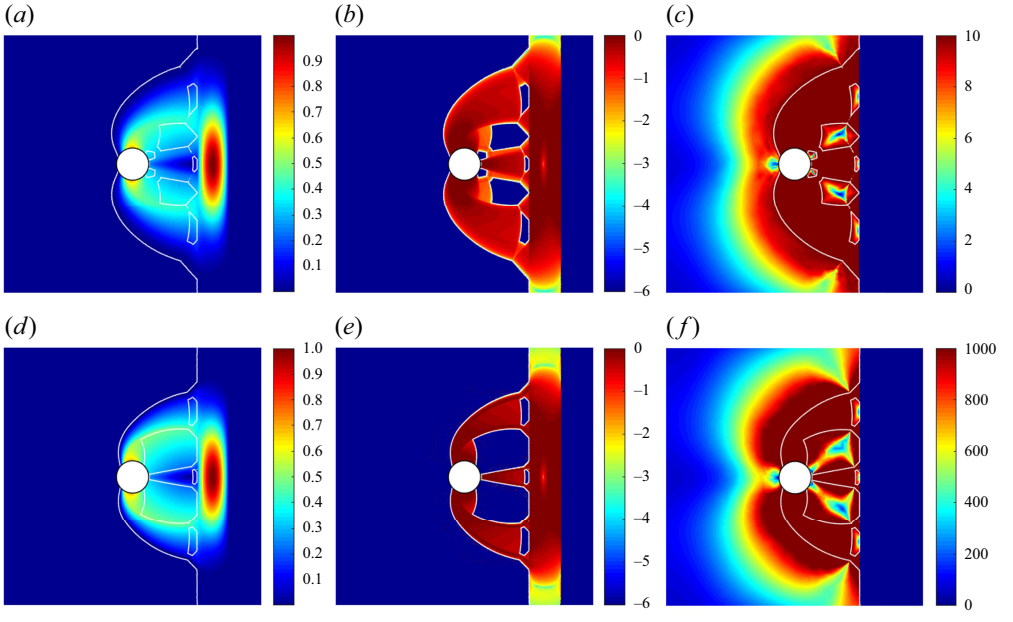


Figure 8. The [R] formulation computations: the magnitude of velocity field (*a*,*d*), strain rate ($\log \|\dot{\boldsymbol{\gamma}}\|$) (*b*,*e*) and deviatoric stress $||\boldsymbol{\tau}||$ (*c*,*f*) contours at $B = 10$ (*a*–*c*) and $B = 1000$ (*d*–*f*) for a circular bubble positioned at offset distance $\Lambda = 3$ to the Newtonian layer; $\gamma_M = 0$.

fine mesh resolution to resolve the sharp gradients in the narrow sheared layers. This in turn requires more mesh adaptivity cycles. In practice, the gain in precision for evaluating Y_c at larger B is minimal.

Zare *et al.* (2021) studied similar viscoplastic systems using a regularised formulation of the constitutive law and reported comparable trends in plug development and flow onset. Regularisation methods tend, however, to smooth out the yield surface transition, suppressing the geometrical features of the exact Bingham model in these limits. They are, however, relatively easy to implement in standard solvers. Even regularisation methods have difficulties at large B as the condition number of the system matrix increases. Hence, the variational inequality approach adopted here enables sharper resolution of yielded versus unyielded regions and offers improved accuracy in capturing the critical yield limit. This improved resolution generally comes at the expense of increased computational cost compared with regularised formulations.

Figure 8 shows the magnitude of velocity, strain rate (in logarithmic scale) and stress fields for a circular bubble positioned at offset $\Lambda = 3$, computed for $B = 10$ and $B = 1000$.

https://doi.org/10.1017/jfm.2026.11637 Published online by Cambridge University Press

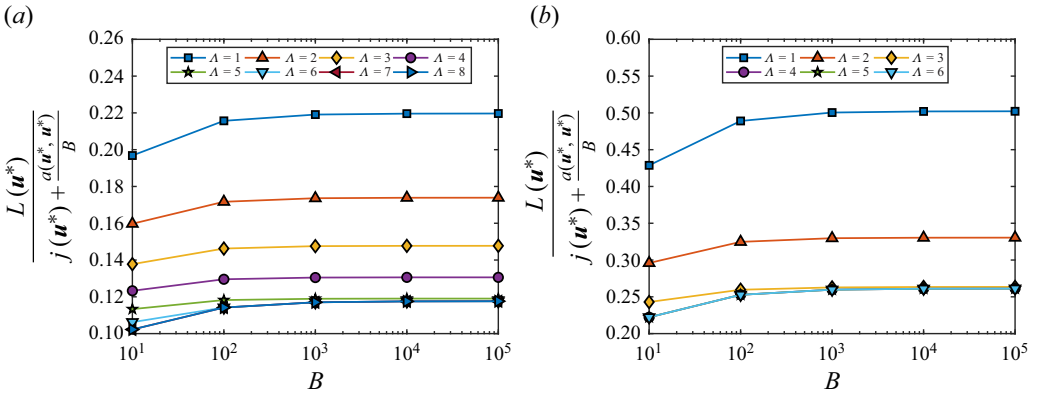


Figure 9. Convergence of computed critical yield number Y_c for elliptical bubbles at various offset distances from a damaged region with no surface tension: (*a*) $\chi = 0.5$ and (*b*) $\chi = 2$.

The velocity field indicates that the symmetry of the uniform viscoplastic medium is broken. The fluid in front of the bubble flows towards the Newtonian layer and towards the bubble behind it. The strain rate contour in figure 8(*b*) highlights the presence of plug regions (areas of unyielded material) surrounding parts of the bubble and extending towards the damaged layer. These regions correspond to zones where the stress is below the yield threshold, resulting in negligible deformation. In the resistance-based formulation, what is being computed is effectively the shape of the velocity field near the onset of motion ($B \to \infty$), normalised by an arbitrarily small mobility velocity. Thus, while the plug regions are rigid, small-scale linear or rotational motion may still occur within them, without being static, e.g. flow is permitted into and out of these regions, while maintaining zero strain rate. The plug structure therefore acts as a stress-transmitting body, bridging the bubble and the nearby Newtonian layer while remaining mechanically undisturbed. Figure 8(*c*) highlights how the bubble-induced stress field overlaps with the damaged region. The analogous $B = 1000$ fields (figure 8*d–f*) show the same qualitative structure, but with sharper yield surfaces and enlarged plug regions, consistent with the high-B limit. It is interesting to speculate on the limit as $B \to \infty$, where the stresses in the Bingham fluid scale with B, but the Newtonian layer cannot match these while remaining static. Is this mathematically equivalent to imposing a stress-free condition along the interface?

4.2. *Effect of bubble aspect ratio*

Next we investigate the influence of bubble aspect ratio χ on the critical yield number Y_c and the critical offset distance Λ_c. We consider only mild elongations $\chi \in [0.5, 2]$, as these are mostly those found in practice. The general trend of Y_c for larger and smaller χ can be inferred from the results of Pourzahedi *et al.* (2022).

Figure 9 shows the convergence of the computed critical yield number Y_c for elliptical bubbles at various offset distances Λ from the damaged region. We can see that the behaviour of the resistance method is similar to that in figure 7, for $\chi = 1$, i.e. increasing to a plateau for large B, at each value of Λ studied. The corresponding asymptotic quantities are listed in tables 3 and 4, with fitting method as before. To compare the decay of Y_c with its value in an infinite domain of homogeneous fluid, we have computed Y_c for a finer mesh of Λ values near to the limit. Figure 10 displays the monotonic decay of Y_c to the plateau $Y_{c,\infty}$. The corresponding values of $Y_{c,\infty}$ approximated and the critical offset distances Λ_c, for the different aspect ratios χ, are summarised in table 5.

https://doi.org/10.1017/jfm.2026.11637 Published online by Cambridge University Press

Λ	Y_c	d	ν
1	0.2197	1.202	0.8315
2	0.1739	1.142	0.8874
3	0.1477	1.121	0.9424
4	0.1306	1.089	0.9550
5	0.1190	1.054	0.9052
6	0.1176	1.130	0.7763
7	0.1176	1.117	0.7524
8	0.1176	1.117	0.7533

Table 3. Asymptotic fit parameters Y_c, d and ν for $\chi = 0.5$, $\gamma_M = 0$.

Λ	Y_c	d	ν
1	0.5022	0.7531	0.8784
2	0.3305	0.3330	0.8816
3	0.2635	0.1155	0.7367
4	0.2613	0.2683	0.7496
5	0.2613	0.2589	0.7410
6	0.2613	0.2614	0.7430

Table 4. Asymptotic parameters Y_c, d and ν for $\chi = 2$, $\gamma_M = 0$.

Aspect ratio χ	0.5	1	2
$Y_{c,\infty}$	0.118	0.171	0.261
Λ_c	5.2	3.9	3.1

Table 5. Computed critical yield number Y_c and critical offset Λ_c for 2-D elliptical bubbles with no surface tension.

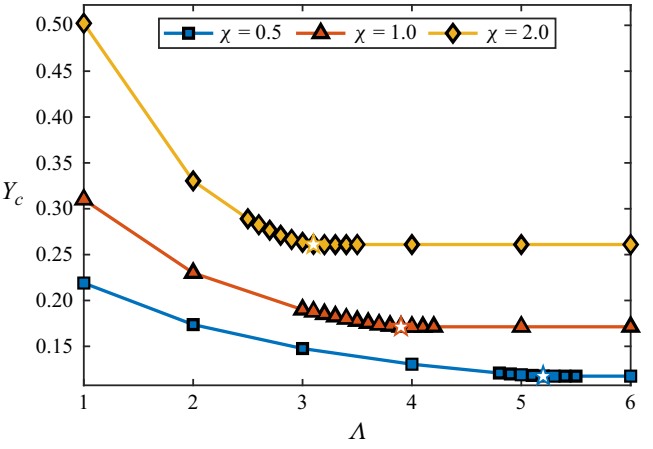


Figure 10. Decay of Y_c to $Y_{c,\infty}$ with Λ for elliptical bubbles of varying χ with no surface tension; ⋆ indicates the critical offset distance.

https://doi.org/10.1017/jfm.2026.11637 Published online by Cambridge University Press

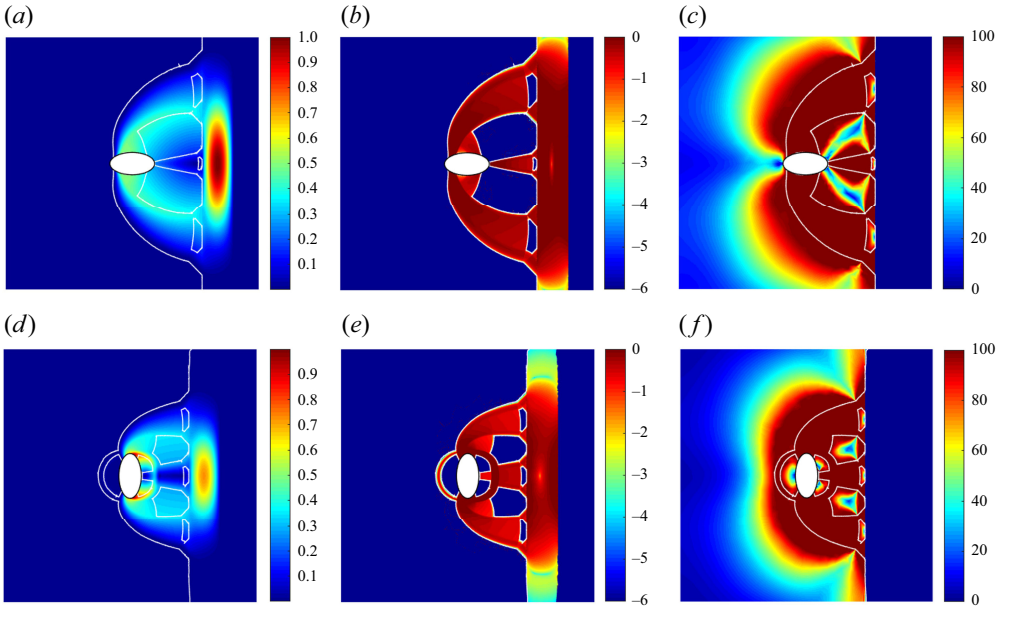


Figure 11. The [R] formulation computations: contours of the magnitude of (*a*,*d*) velocity, (*b*,*e*) strain rate ($\log \|\dot{\boldsymbol{\gamma}}\|$) and (*c*,*f*) deviatoric stress $\|\boldsymbol{\tau}\|$, for an elliptical bubble at $B = 100$ with $\gamma_M = 0$ in close proximity to a damaged pathway with offset distance $\Lambda = 3$. (*a–c*) An oblate bubble ($\chi = 0.5$); (*d–f*) a prolate bubble ($\chi = 2$).

As the bubble becomes more vertically elongated, Y_c increases, indicating that prolate bubbles require a higher yield stress to prevent motion. This arises from sharper curvature near the vertical poles, which enhances local stress concentrations, and from a thicker unyielded plug that forms around the bubble, both of which resist motion. In contrast, oblate bubbles experience weaker confinement and are trapped more easily.

Interestingly, while the critical yield number Y_c increases with χ, the critical offset distance Λ_c decreases monotonically. For the oblate bubble , $\Lambda_c = 5.2$, indicating that the damaged region influences its motion over a relatively long spatial range. For the circular bubble, this distance decreases to $\Lambda_c = 3.9$, and for the prolate bubble it further reduces to $\Lambda_c = 3.1$. These results show that as the bubble elongates vertically, the effect of the damaged region fades more rapidly with horizontal distance. In other words, taller bubbles are less sensitive to heterogeneities away from their central axis, while flattened bubbles remain affected even when the damaged zone is farther away.

To further illustrate this effect, figure 11 compares velocity, strain rate (in logarithmic scale) and stress fields for oblate and prolate bubbles at a fixed offset distance of $\Lambda = 3$. The oblate bubble maintains a broader unyielded plug region along the vertical axis, enhancing confinement and resistance to motion, whereas the prolate bubble exhibits strain localisation near its vertical poles, facilitating yielding and motion despite the horizontal asymmetry.

4.2.1. *The limiting process of [M] and [R] compared*

A significant part of this study has been taken up with finding a robust method of calculating Y_c, which initially appeared a simple matter. Using formulation [R] at increasing values of B leads to a consistent plateau value of Y, which asymptotes to $Y_c = Y_c^{[R]}$, eventually found by fitting. Since every computed $\boldsymbol{u}^*$ also can be rescaled to

https://doi.org/10.1017/jfm.2026.11637 Published online by Cambridge University Press

Functional	ν (R→M)	p (M)
$j(\boldsymbol{u})$	0.9995	1.1413
$a(\boldsymbol{u}, \boldsymbol{u})$	1.9588	2.0575
$L(\boldsymbol{u})$	0.9994	1.1396

Table 6. Power-law exponents for the functionals $j(\boldsymbol{u})$, $a(\boldsymbol{u}, \boldsymbol{u})$ and $L(\boldsymbol{u})$ obtained from the rescaled resistance (R→M) and mobility (M) formulations.

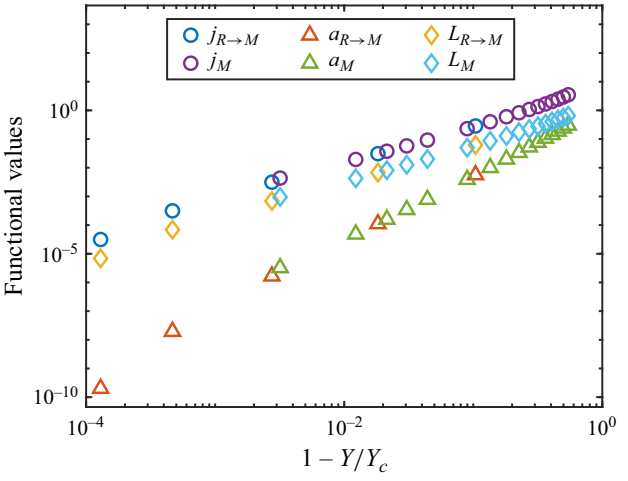


Figure 12. Comparison of rescaled resistance ($R \to M$) and mobility (M) functionals near the critical yield number for an oblate bubble $\chi = 0.5$ positioned at $\Lambda = 1$ with no surface tension.

give $\boldsymbol{u}$, the rescaled resistance functionals may be compared with the mobility functionals, decaying with respect to $1 - Y/Y_c$. Figure 12 shows the comparison of near-critical scaling behaviour, plotting $j(\boldsymbol{u})$ obtained from the resistance [R] and mobility [M] formulations, for $\chi = 0.5$ with no surface tension. The results computed using [R] (rescaled) tend to approach closer to the zero limit than the [M] results. The rescaled [R] functional appears consistent with the [M] values. In other words, figure 12 provides a useful consistency check.

In particular, the resistance results are characterised by the asymptotic fit $\sim B^{-\nu}$ at large B, while the mobility results exhibit near-critical decay of the form $\sim (Y_c - Y)^p$ as $Y \to Y_c^-$. Power-law exponents extracted from these data are summarised in table 6 for the functionals $j(\boldsymbol{u})$, $a(\boldsymbol{u}, \boldsymbol{u})$ and $L(\boldsymbol{u})$. While the fitted exponents differ slightly between the rescaled resistance mapping ([R] → [M]) and the mobility formulation, they are broadly consistent with the expected asymptotic behaviour as $Y \to Y_c^-$. Given the limited asymptotic range accessible in the numerical data, particularly for the mobility formulation, these fits are best interpreted as qualitative indicators of near-critical scaling behaviour rather than as precise quantitative measurements.

4.3. *Surface tension effects*

To assess how surface tension alters the bubble–damage interaction, we repeat the simulations for the same aspect ratios, $\chi = 0.5$ and $\chi = 2$, but with $\gamma_M = 1$. Following the results in Pourzahedi *et al.* (2022), where the surface tension is also represented by

https://doi.org/10.1017/jfm.2026.11637 Published online by Cambridge University Press

Λ	Y_c	d	ν
1	0.3829	1.249	0.8006
2	0.3257	0.9817	0.6539
3	0.3258	0.9746	0.6518
4	0.3258	0.9609	0.6487

Table 7. Asymptotic fit parameters Y_c, d and ν for $\chi = 0.5$, $\gamma_M = 1$.

Λ	Y_c	d	ν
1	0.6803	3.885	0.8658
2	0.4501	2.011	0.8911
3	0.4027	2.240	0.7856
4	0.4027	2.206	0.7810
5	0.4026	2.225	0.7839

Table 8. Asymptotic fit parameters Y_c, d and ν for $\chi = 2$, $\gamma_M = 1$.

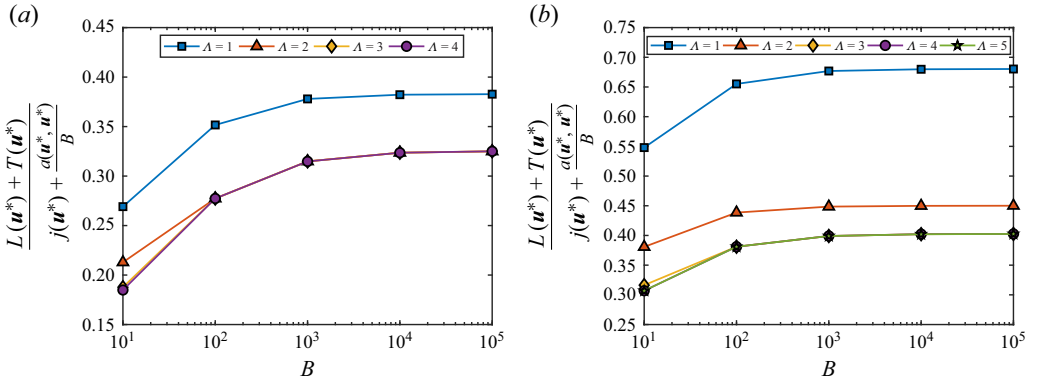


Figure 13. Convergence of computed critical yield number Y_c for elliptical bubbles at various offset distances from a damaged region with $\gamma_M = 1$: (*a*) $\chi = 0.5$ and (*b*) $\chi = 2$.

γ_M, we expect to see significant effects at this value. At more extreme values of χ it has also been observed that surface tension can become dominant over buoyancy due to the high curvature of the points of the ellipse. However, extremely long bubbles also tend to deform and break up when mobilised, so we keep the parameter range restricted.

Figure 13 shows examples of convergence of $Y \to Y_c$ at large B, essentially showing the same qualitative behaviour as in previous plots. The corresponding asymptotic values for $\gamma_M = 1$ are reported in tables 7 and 8. A very clear effect of surface tension is found in the values of Y_c, i.e. compare the limiting values in figure 13 with those earlier in figure 9. This arises due to the need for the yield stress to resist not only the buoyancy forces but also the surface-tension-induced stresses.

Velocity, strain-rate and stress contours are plotted in figure 14. Surprisingly, the surface tension tends to smooth the distribution of strain rate around the bubble, particularly near the interface between the bubble and the damaged region. For both aspect ratios, the presence of surface tension appears to confine the deformation and localises strain rates

https://doi.org/10.1017/jfm.2026.11637 Published online by Cambridge University Press

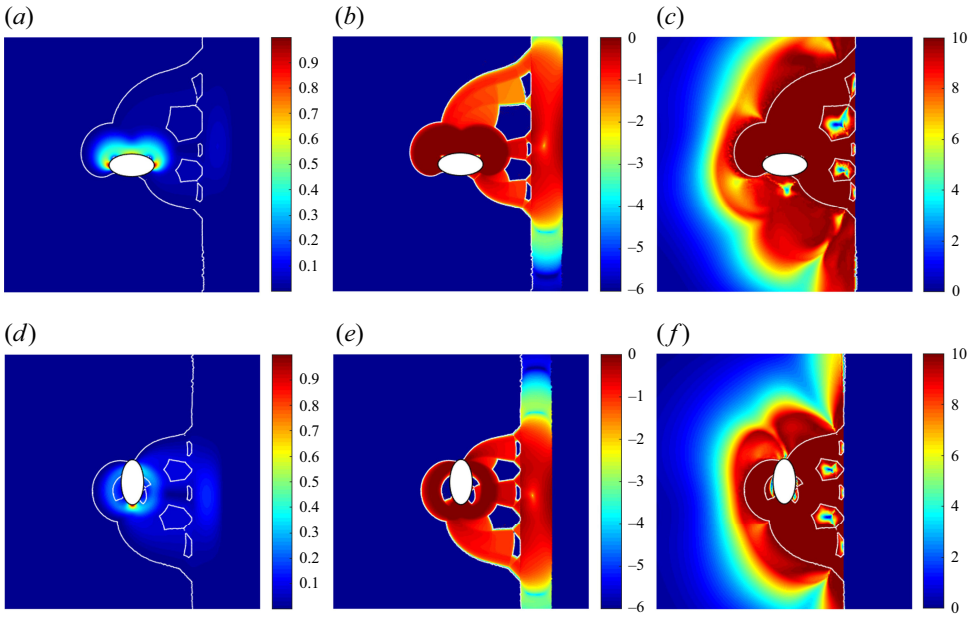


Figure 14. The [R] contours of the magnitude of (*a*,*d*) velocity, (*b*,*e*) strain rate ($\log \|\dot{\boldsymbol{\gamma}}\|$) and (*c*,*f*) deviatoric stress $||\boldsymbol{\tau}||$, for an elliptical bubble at $B = 10$ with $\gamma_M = 1$ in close proximity to a damaged pathway with offset distance $\Lambda = 3$. (*a–c*) An oblate bubble ($\chi = 0.5$); (*d–f*) a prolate bubble ($\chi = 2$).

near the bubble edge. This enhanced interfacial stability appears to weaken the mechanical coupling between the bubble and the surrounding damaged layer. The other obvious effect in figure 14 is the loss of fore–aft symmetry about the bubble.

Quantitatively, in the absence of surface tension, oblate bubbles ($\chi = 0.5$) interact with the damaged layer up to $\Lambda_c \approx 5.2$, while prolate bubbles ($\chi = 2$) do so up to $\Lambda_c \approx 3.1$. When surface tension is included, these interaction distances decrease to $\Lambda_c \approx 1.6$ and $\Lambda_c \approx 2.5$, respectively. The reduction is more pronounced for the oblate bubble. This arises because oblate bubbles have their points of highest curvature in the direction of the damaged layer, resulting in larger surface tension pressure jumps. This more strongly suppresses interfacial deformation and shields the surrounding material from stress transmission.

Despite this overall reduction in Λ_c, prolate bubbles continue to feel the damaged region from slightly farther away than oblate ones. Their elongated geometry promotes sharper stress gradients near the poles, which enhances local yielding and enables deeper penetration of stresses into the surrounding fluid. These findings highlight the dual role of surface tension in damaged viscoplastic environments: while it generally limits the spatial extent of bubble–damage interaction, it simultaneously modifies the balance between geometric and interfacial effects governing the onset of motion.

4.4. *Viscosity ratio effect on the critical yield number*

Having examined the influence of geometric and interfacial parameters, we next investigate whether the viscosity contrast between the damaged and undamaged regions affects the onset of bubble motion. The viscosity ratio $\mu = \hat{\mu}_N/\hat{\mu}_p$ was varied over several orders of magnitude to assess its influence on the critical yield number Y_c.

As shown in figure 15, variations in μ have a negligible effect on Y_c. This result confirms that the onset of motion is governed by the yield stress and plastic dissipation, rather than

https://doi.org/10.1017/jfm.2026.11637 Published online by Cambridge University Press

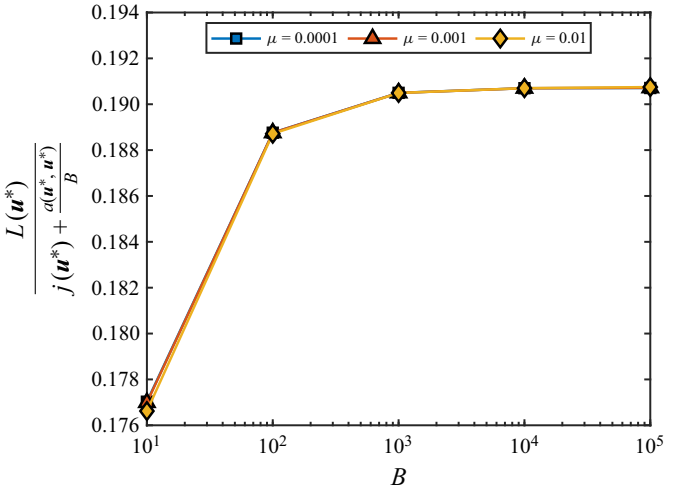


Figure 15. Critical yield number Y_c as a function of viscosity ratio μ_N/μ_P. Results are shown for fixed bubble aspect ratio $\chi = 1$, offset distance $\Lambda = 3$ and surface tension $\gamma_M = 0$. Despite orders-of-magnitude variation in the Newtonian viscosity, Y_c remains effectively unchanged, confirming that yield stress distribution, not viscous dissipation, governs the onset of motion.

by viscous dissipation within the yielded zones. In other words, flow initiation occurs when the applied stress first exceeds the yield stress locally, and this condition is largely insensitive to the viscosity of the Newtonian (damaged) region. This insensitivity to the viscosity ratio is consistent with the asymptotic limit $B \to \infty$, in which the interfacial traction tends to zero and the influence of the Newtonian layer becomes secondary.

This observation is consistent with the physics of Stokes flow in viscoplastic systems. As in our study of the energy balance, close to flow onset, onset of motion depends on the balance of (linear) functionals representing buoyancy and surface tension, with the plastic dissipation. The viscous terms in the balance converge faster to zero and so should not affect the balance. Although non-zero shear stresses are transmitted from the yield-stress fluid into the adjacent Newtonian layer, these stresses are themselves independent of μ_N. Modifying the Newtonian viscosity therefore affects only the local velocity gradients, without altering the overall stress distribution. Near Y_c, the shear stresses in the Newtonian layer remain extremely small, rendering strain rates negligible regardless of viscosity. The damaged layer behaves effectively as a passive, low-resistance conduit that does not influence the critical yield number through its viscosity.

4.5. *Horizontal velocity*

To further explore the effects of the damaged region, the mean horizontal velocity component of the bubble $\bar{u}_x$ is computed, by averaging the horizontal fluid velocity and using incompressibility. We do this for values of $Y < Y_c$, in order that there is bubble motion. The results presented are mainly qualitative, to gain insight into the size of these effects, as the calculations we perform are steady-Stokes-flow calculations, i.e. our results indicate only the velocities for a specific instant and shape, but do not evolve in time.

Initially we start with $\gamma_M = 0$. We fix Y to be 90 % of the critical value, i.e. $Y = 0.9Y_c(\Lambda)$, for values of $\Lambda = 1,\ 2,\ 3$. For each Y we expect the bubble to be in motion for $\Lambda = 1$. As the offset distance increases we expect the influence of the damaged layer to decrease until eventually the bubble rises vertically, but at larger Λ note that Y_c also decreases. The results are shown in figure 16.

https://doi.org/10.1017/jfm.2026.11637 Published online by Cambridge University Press

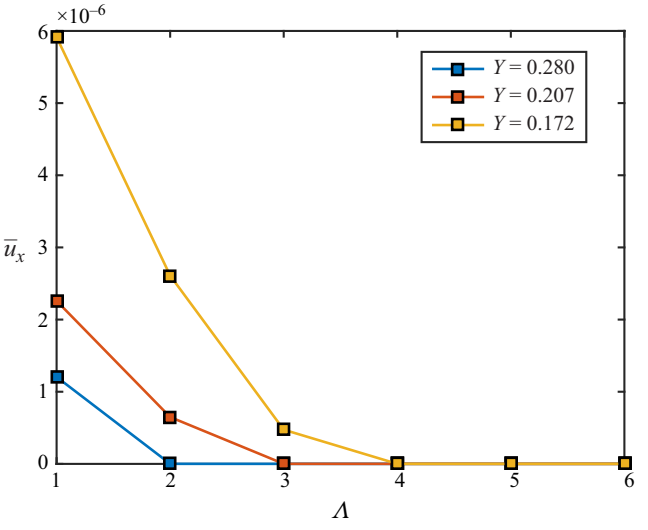


Figure 16. Decay of the horizontal bubble velocity $\bar{u}_x$ with Λ for three values of Y ($\chi = 1$, $\gamma_M = 0$).

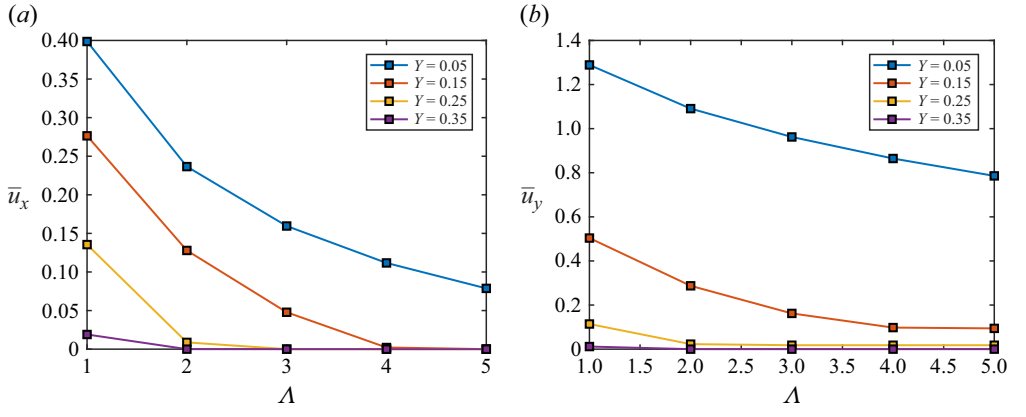


Figure 17. Decay of the mean bubble velocities with Λ for an oblate bubble ($\chi = 0.5$, $\gamma_M = 1$). (*a*) Horizontal velocity $\bar{u}_x$. (*b*) Bubble rise velocity $\bar{u}_y$.

Figure 16 shows that the horizontal bubble velocity $\bar{u}_x$ decays to zero at a fixed distance from the damaged layer. This distance is shorter for larger Y. We see that in each case the horizontal component of velocity is effectively zero at large Λ: here $\Lambda = 5$ suffices. The critical limit for the circular bubble at large Λ is $Y_{c,\infty} = 0.1715$, so that each Y value explored should lead to zero velocity at large Λ. The other main comment related to figure 16 is that the horizontal velocities for the case $\gamma_M = 0$ are remarkably small.

We now consider effects on $\bar{u}_x$ for oblate ($\chi = 0.5$) and prolate ($\chi = 2$) bubbles, each at fixed surface tension parameter $\gamma_M = 1$. Again we fix the yield number Y and vary the offset distance Λ over the range $1 \leqslant \Lambda \leqslant 5$. We consider a wide range of Y, for which the bubble can remain mobile for all Λ.

Figures 17 and 18 show the variation of $\bar{u}_x$ and the corresponding mean rise velocity $\bar{u}_y$ with Λ. Physically, as the offset distance increases, the influence of the damaged layer weakens and the bubble motion is expected to become increasingly vertical. For example, in figure 17 at $Y = 0.15$ the vertical velocity $\bar{u}_y \approx 0.1$ at $\Lambda \gtrapprox 4$, while $\bar{u}_x$ has effectively

https://doi.org/10.1017/jfm.2026.11637 Published online by Cambridge University Press

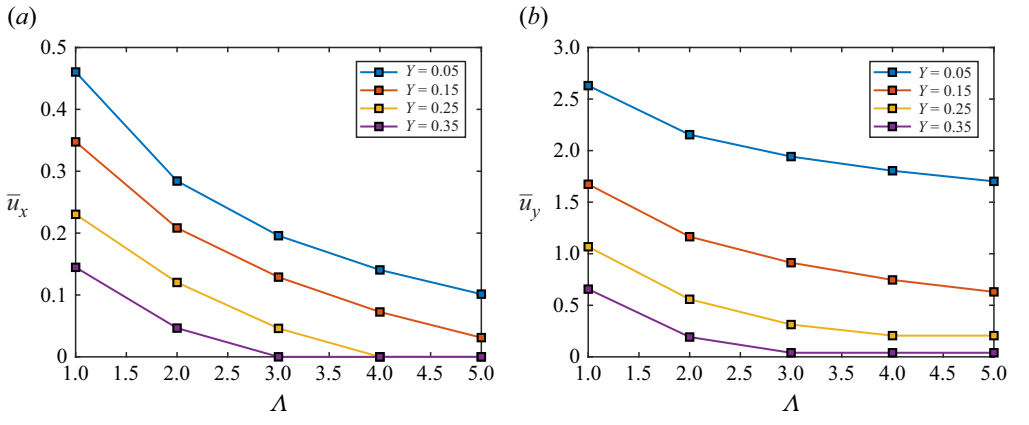


Figure 18. Decay of the mean bubble velocities with Λ for a prolate bubble ($\chi = 2$, $\gamma_M = 1$). (*a*) Horizontal velocity $\bar{u}_x$. (*b*) Bubble rise velocity $\bar{u}_y$.

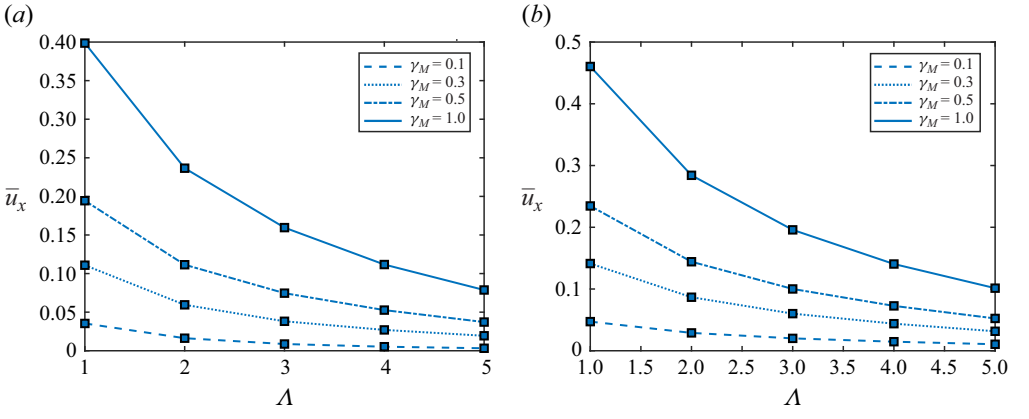


Figure 19. Decay of the mean horizontal velocities with Λ at fixed $Y = 0.05$ for different values of surface tension: (*a*) $\chi = 0.5$; (*b*) $\chi = 2$.

vanished. Note that $Y_{c,\infty} = 0.3258$ for this geometry and γ_M, so curves except that for $Y = 0.35$ converge to a non-zero rise velocity at large Λ.

In all cases, the horizontal velocity decreases monotonically with increasing Λ, approaching zero once the bubble is sufficiently far from the damaged layer. This decay occurs more rapidly for larger yield numbers, reflecting the stronger resistance of the surrounding material. For the parameter ranges shown, $\Lambda = 5$ leads to a substantial reduction in $\bar{u}_x$ at large yield numbers, indicating that the influence of the damaged region on the bubble dynamics becomes much weaker at this distance.

The corresponding vertical rise velocities $\bar{u}_y$ also decrease with increasing Λ, though more gradually. This reflects the reduction in the stress asymmetry induced by the damaged layer as the offset distance increases. At fixed Λ, both $\bar{u}_x$ and $\bar{u}_y$ also decrease with increasing Y, consistent with the increasing resistance of the viscoplastic material. The values of $\bar{u}_x$ computed in figures 17 and 18 are notably larger than those for the earlier circular bubble ($\chi = 1$) in figure 16. It might be questioned whether this is due to the different shape or to surface tension.

Figure 19 isolates the effect of surface tension by showing $\bar{u}_x$ as a function of Λ at fixed $Y = 0.05$ for several values of γ_M, for both $\chi = 0.5$ and $\chi = 2$. Increasing surface

https://doi.org/10.1017/jfm.2026.11637 Published online by Cambridge University Press

tension leads to systematically larger horizontal velocities at small Λ, while preserving the same qualitative decay with offset distance. In all cases, $\bar{u}_x$ tends to zero as Λ increases, confirming that surface tension modifies the magnitude of the lateral motion but not its overall dependence on the offset distance. Other computations (not shown) reveal that bubble shape has a much smaller effect on the lateral velocity than does γ_M.

Overall, the results of this section demonstrate that lateral bubble motion is a near-field effect associated with proximity to the damaged layer. Once the bubble is sufficiently far from this region, its motion becomes essentially vertical, independent of yield number, aspect ratio or surface tension.

5. Summary and conclusions

Various experimental studies (see § 1) over the past 30 years have suggested that viscoplastic fluids retain memory of the passage of buoyant objects through them (particles, bubbles, etc.), long after the usual relaxation times that might be associated with the elastic response of such systems. This memory manifests by allowing subsequent objects to move faster along the same pathways and by attracting nearby objects towards the pathways. While a full rheological characterisation and explanation for these effects is lacking, one can at least study the effects of a weakened pathway on nearby flow behaviour using an idealised system. This has been the goal of our study, in which we have explored a 2-D flow consisting of a bubble in a Bingham fluid that contains a weakened vertical layer of Newtonian fluid. As principally we study flow onset, the results generated for the Bingham fluid are equally valid for other similar models, Herschel–Bulkley, Casson, etc., which provides some wider generality. The Bingham fluid is inelastic, remaining undeformed for stresses below a given yield stress, which allows bubbles below a critical size to be trapped within the fluid. The problem studied here revolves around release of trapped bubbles and how the flow onset limit is affected by the damaged Newtonian layer. The fact that it is influenced, in the absence of elasticity, suggests a strong role for the stresses in the static fluid. Note that in unyielded fluid regions, although the stresses are not uniquely determined by the constitutive relation, they are constrained by the Stokes equations, which serve as equilibrium conditions.

We have worked with an AL framework to study the onset of motion, as this method allows for truly rigid areas of flow under an applied stress. Our initial results using a mobility formulation have difficulties in properly quantifying the flow onset. Thus, instead we moved to a resistance formulation, in which the mean bubble rise velocity is imposed. This results in the flow onset being captured via a critical value of yield number (Y_c), which is robustly calculated as the limiting value of the functional (3.20), evaluated for the velocity solution, as the Bingham number $B \to \infty$. We have found that Y_c is sensitive to various geometric parameters, explored in the paper.

First, our results confirm that the presence of a damaged region strongly modifies Y_c. When the bubble is sufficiently close to the Newtonian channel, the stress fields overlap and form a lubricated bridge that allows motion at yield numbers considerably higher than the critical limit for a bubble in a uniform Bingham fluid. As the distance of the bubble from the Newtonian damaged path increases, the coupling between the bubble and the damaged pathway weakens. Beyond a critical offset ($\Lambda_c \approx 3.9$, for the circular bubble), the damaged layer no longer influences the onset of motion. This critical distance provides a simple quantitative measure of the spatial extent over which prior damage affects subsequent bubble rise. Consequently, one can estimate the bubble fraction below which a distribution of bubbles is likely to be affected by adjacent bubbles.

https://doi.org/10.1017/jfm.2026.11637 Published online by Cambridge University Press

The dependence of the critical distance Λ_c on bubble shape is also pronounced: oblate bubbles experience weaker confinement and thus a smaller Y_c is sufficient. However, their interaction with the damaged layer extends over larger distances. Prolate bubbles, in contrast, exhibit higher yield limits but reduced sensitivity to lateral non-uniformities. Surface tension further limits the coupling between the bubble and the damaged layer, shrinking the influence range from its capillarity-free value. Lastly, the viscosity contrast between the Newtonian and viscoplastic regions has negligible influence on Y_c, confirming that flow initiation is governed primarily by the buoyancy-induced stress distribution balancing with the yield stress, and not by viscous stresses within the yielded zones.

A nearby damaged layer also induces lateral bubble migration over a finite range of offset distances, with the mean horizontal velocity decaying monotonically as the separation increases and becoming negligible once the bubble is sufficiently far from the weakened region. These qualitative features are similar to those observed in the recent experimental study of Goral & Frigaard (2025), in which a simple toy model was developed, based on a stress deficit close to a damaged layer. This was used to fit the horizontal bubble velocity observed. Computations such as those here provide a different way of developing similar predictions and perhaps calibrating for surface tension and shape effects. In this context, it is notable that the lateral bubble velocities computed appear insignificant without surface tension.

While the above paragraphs summarise the main results established for our model problem, we should also consider their applicability to real fluid systems. In considering laboratory-scale experiments with model transparent fluids, two considerations must be made: (i) rheological and (ii) dimensional. Regarding rheological limitations, what our model formulation provides is a general framework for analysing flow onset in heterogeneous viscoplastic media. Beyond the specific problem of bubble entrapment, it offers a methodology for characterising critical states in systems where localised rheological softening or prior yielding introduces non-uniformity, although it does not model the creation of non-uniformity. Modelling the creation of the non-uniformity would be possible with some EVP or thixotropic models of yield-stress fluids. For a laboratory-scale fluid experiment, with common transparent viscoplastic fluids, this might be a sensible next step. However, common EVP models have not been formulated to focus on elastic creep and plastic yielding. There is also ongoing discussion regarding the role of thixotropy in these fluids and how to model.

Our eventual hope for application is to build network-like models that characterise the likely subsurface stress-pathway structure in tailings ponds or natural mud systems. These structures in turn control the larger-scale stability of ponds/lakes and susceptibility to large-scale bubble release. Regarding dimensional considerations, the concern is that our 2-D results model a rising elliptical (or circular) cylinder close to a plane channel of Newtonian fluid. Evidently, the question arises as to the relevance of the 2-D results for actual 3-D scenarios. The first concern is that in Stokes flow and elasticity, spatial disturbances lead to stresses that decay more slowly in two dimensions than in three dimensions, typically as $1/r$ rather than $1/r^2$.

There are two features to examine here: creation of a damaged structure and the later proximity of a bubble to the damaged structure. For creation, we should note that our physical intuition concerning stress decay refers to an instantaneous Stokes flow around a particle or bubble. However, in the damaging phase this particle/bubble translates (mostly vertically), shearing the fluid in a cylinder around its path. The distance from the surface of the object to the outer radius of the yielded envelope, while in motion, is typically a few radii. Pourzahedi *et al.* (2022) show illustrative results for axisymmetric ellipsoids and

https://doi.org/10.1017/jfm.2026.11637 Published online by Cambridge University Press

planar ellipses, which have comparable extent at 90 % of Y_c, and also vary qualitatively in similar ways with physical problem parameters. Thus, if yielded envelope is taken as an indicator of the size of damaged layer, results based on a planar computation are likely reasonable approximations. Experimentally, perhaps most relevant is the study of Mougin *et al.* (2012) (see their figure 17 and discussion), which shows that outside of the actual bubble path, a narrow region is also sheared, but then beyond that fluid particles are merely displaced and returned to their initial positions, after the bubble has passed. This suggests an elastically strained cylindrical region of damage, comparable to the yielded envelope in extent.

Of course, not all damage/creation is cylindrical. It is interesting that in Goral & Frigaard (2025), where a planar surface is inserted and removed from the fluid to damage it, there is still a finite distance beyond which the effects are not felt, i.e. here path creation is 2-D, but the damage extends still a finite distance. There are other examples of stress heterogeneity effects in Mougin *et al.* (2012) and Lopez *et al.* (2018), with different geometric origins. In an industrial tailings pond setting, we may also expect larger-scale heterogeneity due to, for example, addition of new material, varying bottom topography, stirring/purging, freeze–thaw cycles. Thus, damaged structures within a bond are likely to combine both previous bubble pathways and other features

Regarding proximity of bubbles to a damaged feature, the main point to note is that the computed critical distances Λ_c are necessarily larger than the yielded envelopes around the bubble, including in the limit as $Y \to Y_c$ in an infinite domain ($\Lambda \to \infty$). Yielded envelopes only reflect the position where the yield stress is attained. Beyond the envelope, the stress continues to decay. Due to the yield stress, it is not necessary for $r \to \infty$ in order for the stress field to have insignificant effect on the flow. We have seen this here and it appears true in three dimensions and in the experiments of Goral & Frigaard (2025). In other words, since only decay over finite distances appears necessary, the supposed decay differences between $\sim 1/r$ and $\sim 1/r^2$, at distances $r \sim 1$, are not crucial. We believe that our results can be safely interpreted as identifying qualitative trends and mechanisms, as well as parametric effects, although not precise 3-D values.

Acknowledgements. The authors acknowledge helpful discussions with E. Chaparian and M. Zare during the course of this research and thank the reviewers for raising interesting questions.

Funding. The authors gratefully acknowledge the financial support of NSERC from the excellent Discovery grant programme (grant number RGPIN-2020-04471): keeping Canadian research strong and free!

Declaration of interests. The authors report no conflict of interest.

References

Atapattu, D.D., Chhabra, R.P. & Uhlherr, P.H.T. 1995 Creeping sphere motion in Herschel-Bulkley fluids: flow field and drag. *J. Non-Newtonian Fluid Mech.* **59** (2–3), 245–265.

Balmforth, N., Frigaard, I.A. & Ovarlez, G. 2014 Yielding to stress: recent developments in viscoplastic fluid mechanics. *Annu. Rev. Fluid Mech.* **46** (1), 121–146.

Bussmann, I., Schlömer, S., Schlüter, M. & Wessels, M. 2011 Active pockmarks in a large lake (Lake Constance, Germany): effects on methane distribution and turnover in the sediment. *Limnol. Oceanogr.* **56** (1), 379–393.

Chaparian, E. & Frigaard, I.A. 2017 Yield limit analysis of particle motion in a yield-stress fluid. *J. Fluid Mech.* **819**, 311–351.

Chaparian, E. & Frigaard, I.A. 2021 Clouds of bubbles in a viscoplastic fluid. *J. Fluid Mech.* **927**, R3.

Chaparian, E., Wachs, A. & Frigaard, I.A. 2018 Inline motion and hydrodynamic interaction of 2D particles in a viscoplastic fluid. *Phys. Fluids* **30**, 033101.

Daneshi, M. & Frigaard, I.A. 2023 Growth and stability of bubbles in a yield stress fluid. *J. Fluid Mech.* **957**, A16.

https://doi.org/10.1017/jfm.2026.11637 Published online by Cambridge University Press

DANESHI, M. & FRIGAARD, I.A. 2024 Growth and static stability of bubble clouds in yield stress fluids. *J. Non-Newtonian Fluid Mech.* **327**, 105217.
DERAKHSHANDEH, B. 2016 Kaolinite suspension as a model fluid for fluid dynamics studies of fluid fine tailings. *Rheol. Acta* **55** (9), 749–758.
DIMAKOPOULOS, Y., PAVLIDIS, M. & TSAMOPOULOS, J. 2013 Steady bubble rise in Herschel–Bulkley fluids and comparison of predictions via the augmented Lagrangian method with those via the Papanastasiou model. *J. Non-Newtonian Fluid Mech.* **200**, 34–51.
DUBASH, N. & FRIGAARD, I.A. 2004 Conditions for static bubbles in viscoplastic fluids. *Phys. Fluids* **16** (12), 4319–4330.
DUBASH, N. & FRIGAARD, I.A. 2007 Propagation and stopping of air bubbles in Carbopol solutions. *J. Non-Newtonian Fluid Mech.* **142** (1–3), 123–134.
EKELAND, I. & TEMAM, R. 1999 *Convex Analysis and Variational Problems*. SIAM.
ESPOSITO, G., DIMAKOPOULOS, Y. & TSAMOPOULOS, J. 2025 Rising and migration dynamics of an air bubble close to a wall in an elastoviscoplastic fluid. *J. Non-Newtonian Fluid Mech.* **345**, 105482.
GHEISSARY, G. & VAN DEN BRULE, B.H.A.A. 1996 Unexpected phenomena observed in particle settling in non-Newtonian media. *J. Non-Newtonian Fluid Mech.* **67**, 1–18.
GLOWINSKI, R., LIONS, J.L. & TREMOLIERES, R. 1981 Numerical analysis of variational inequalities. *Stud. Maths Applics* **8**, 1–776.
GORAL, M. & FRIGAARD, I.A. 2025 Tuning bubble trajectories in a yield stress fluid. *Phys. Fluids* **37** (4), 043127.
HAJIEGHRARY, O. & FRIGAARD, I.A. 2024 Trapping of bubbles in oil sands tailing ponds. *Energies* **17** (19), 4943.
HE, M. *et al.* 2024 Total organic carbon measurements reveal major gaps in petrochemical emissions reporting. *Science* **383** (6681), 426–432.
HECHT, F. 2012 New development in freefem++. *J. Numer. Maths* **20** (3–4), 251–266.
KAPUR, P.C., SCALES, P.J., BOGER, D.V. & HEALY, T.W. 1997 Yield stress of suspensions loaded with size distributed particles. *AIChE J.* **43** (5), 1171–1179.
LAWRENCE, G.A., TEDFORD, E.W. & PIETERS, R. 2016 Suspended solids in an end pit lake: potential mixing mechanisms. *Can. J. Civil Engng* **43** (3), 211–217.
LIU, S., MULLER, S. & DENN, M. 2003 Interactions of two rigid spheres translating collinearly in creeping flowin a Bingham material. *J. Non-Newtonian Fluid Mech.* **113**, 49–67.
LOPEZ, W.F., NACCACHE, M.F. & DE SOUZA MENDES, P.R. 2018 Rising bubbles in yield stress materials. *J. Rheol.* **62** (1), 209–219.
MOSCHOPOULOS, P., SPYRIDAKIS, A., VARCHANIS, S., DIMAKOPOULOS, Y. & TSAMOPOULOS, J. 2021 The concept of elasto-visco-plasticity and its application to a bubble rising in yield stress fluids. *J. Non-Newtonian Fluid Mech.* **297**, 104670.
MOUGIN, N., MAGNIN, A. & PIAU, J.M. 2012 The significant influence of internal stresses on the dynamics of bubbles in a yield stress fluid. *J. Non-Newtonian Fluid Mech.* **171**, 42–55.
PIETTE, J., MOUD, A.A., POISSON, J., DERAKHSHANDEH, B., HUDSON, Z.M. & HATZIKIRIAKOS, S.G. 2022 Rheology of mature fine tailings. *Phys. Fluids* **34** (6), 063104.
POURZAHEDI, A., CHAPARIAN, E., ROUSTAEI, A. & FRIGAARD, I.A. 2022 Flow onset for a single bubble in a yield-stress fluid. *J. Fluid Mech.* **933**, A21.
PRAGER, W. 1954 On slow visco-plastic flow. In *Studies in Mathematics and Mechanics: Presented to Richard Von Mises by Friends, Colleagues, and Pupils*, p. 208. Academic Press.
PUTZ, A. & FRIGAARD, I.A. 2010 Creeping flow around particles in a Bingham fluid. *J. Non-Newtonian Fluid Mech.* **165** (5–6), 263–280.
ROQUET, N. & SARAMITO, P. 2003 An adaptive finite element method for Bingham fluid flows around a cylinder. *Comput. Meth. Appl. Mech. Engng* **192** (31–32), 3317–3341.
SARAMITO, P. 2007 A new constitutive equation for elastoviscoplastic fluid flows. *J. Non-Newtonian Fluid Mech.* **145** (1), 1–14.
SARAMITO, P. 2009 A new elastoviscoplastic model based on the Herschel–Bulkley viscoplastic model. *J. Non-Newtonian Fluid Mech.* **158** (1–3), 154–161.
SCALES, P.J., JOHNSON, S.B., HEALY, T.W. & KAPUR, P.C. 1998 Shear yield stress of partially flocculated colloidal suspensions. *AIChE J.* **44** (3), 538–544.
SIKORSKI, D., TABUTEAU, H. & DE BRUYN, J.R. 2009 Motion and shape of bubbles rising through a yield-stress fluid. *J. Non-Newtonian Fluid Mech.* **159** (1–3), 10–16.
SMALL, C., CHO, S., HASHISHO, Z. & ULRICH, A. 2015 Emissions from oil sands tailings ponds: review of tailings pond parameters and emission estimates. *J. Petrol. Sci. Engng* **127**, 490–501.

https://doi.org/10.1017/jfm.2026.11637 Published online by Cambridge University Press

TEDFORD, E.W., ZHAO, K., OLSTHOORN, J., PIETERS, R. & LAWRENCE, G.A. 2019 Spatial variability of methane bubbles in lake ice. In *AGU Fall Meeting Abstracts*, vol. 2019, pp. B43I–2589. American Geophysical Union.

TRESKATIS, T., ROUSTAEI, A., FRIGAARD, I.A. & WACHS, A. 2018 Practical guidelines for fast, efficient and robust simulations of yield-stress flows without regularisation: a study of accelerated proximal gradient and augmented Lagrangian methods. *J. Non-Newtonian Fluid Mech.* **262**, 149–164.

TSAMOPOULOS, J., DIMAKOPOULOS, Y., CHATZIDAI, N., KARAPETSAS, G. & PAVLIDIS, M. 2008 Steady bubble rise and deformation in Newtonian and viscoplastic fluids and conditions for bubble entrapment. *J. Fluid Mech.* **601**, 123–164.

WANG, C., HARBOTTLE, D., LIU, Q. & XU, Z. 2014 Current state of fine mineral tailings treatment: a critical review on theory and practice. *Miner. Engng* **58**, 113–131.

WANG, Z., LOU, W., SUN, B., PAN, S., ZHAO, X. & LIU, H. 2019 A model for predicting bubble velocity in yield stress fluid at low Reynolds number. *Chem. Engng Sci.* **201**, 325–338.

WELLS, P.S. & KAMINSKY, H.A.W. 2015 Slurry to soil clay behaviour model: using methylene blue to cross the process/geotechnical engineering divide. In *Conference Proceedings of Tailings and Mine Waste 2015, Vancouver, BC, October 26 to 28, 2015*.

ZARE, M., DANESHI, M. & FRIGAARD, I.A. 2021 Effects of non-uniform rheology on the motion of bubbles in a yield-stress fluid. *J. Fluid Mech.* **919**, A25.

ZARE, M. & FRIGAARD, I.A. 2018 Onset of miscible and immiscible fluids' invasion into a viscoplastic fluid. *Phys. Fluids* **30** (6), 063101.

ZARE, M., FRIGAARD, I.A. & LAWRENCE, G.A. 2024 Bubble-induced entrainment at viscoplastic–Newtonian interfaces. *J. Fluid Mech.* **987**, A28.

ZHAO, K., TEDFORD, E.W., ZARE, M., FRIGAARD, I.A. & LAWRENCE, G.A. 2022 Bubbles rising through a layer of Carbopol capped with water. *J. Non-Newtonian Fluid Mech.* **300**, 104700.

ZHAO, K., TEDFORD, E.W., ZARE, M. & LAWRENCE, G.A. 2021 Impact of atmospheric pressure variations on methane ebullition and lake turbidity during ice-cover. *Limnol. Oceanogr. Lett.* **6** (5), 253–261.

https://doi.org/10.1017/jfm.2026.11637 Published online by Cambridge University Press